Wave propagation through a stationary field of clouds: a homogenization approach

E. J. Goldsmith[a] and J. G. Esler[b]

[a] *Department of Mathematics, University of California, Davis, Davis, California*

[b] *Department of Mathematics, University College London, London, United Kingdom*

Corresponding author: E. J. Goldsmith, ejgoldsmith@ucdavis.edu

ABSTRACT: A new approach to the closure of sub-grid scale cloud fields in the parameterization of convection in large-scale atmospheric models, based upon the asymptotic theory of homogenization, is presented. A key aim is to quantify potential model errors in wave propagation speeds, introduced by using averaged fields in place of the fully resolved circulation, in the setting of a simple stratified Boussinesq mid-latitude β-channel model. The effect of the cloud field, represented here by a random array of strongly nonlinear axisymmetric circulations, is found to appear in the large-scale governing equations through new terms which redistribute the large-scale buoyancy and horizontal momentum fields in the vertical. These new terms, which have the form of non-local integral operators, are linear in the cloud number density, and are fully determined by the solution of a linear elliptic equation known as a cell problem. The cell problem in turn depends upon the details of the nonlinear cloud circulations. The integral operators are calculated explicitly for example cloud fields and then dispersion relations are compared for different waves in the presence of clouds at realistic densities. The main finding is that baroclinic Rossby waves are significantly slowed and damped by the clouds, most strongly at the lowest frequencies. In contrast, Rossby waves with barotropic structure, and all inertia-gravity waves, are found to be almost unaffected by the presence of clouds, even at the highest realistic cloud densities.

1. Introduction

Accurately representing small-scale convective processes within the large-scale framework of global circulation models (GCMs) and numerical weather simulations is one of the most challenging problems within the atmospheric sciences (Arakawa 2004). Since atmospheric convection is a highly turbulent process resulting in momentum and buoyancy fluxes which vary on horizontal scales of less than one kilometre, it cannot be resolved on the larger scale numerical grids used in GCMs (e.g. Collins et al. 2013). Instead, convective parameterizations are used to model the effects of the unresolved processes, allowing large-scale models to reproduce many convectively coupled atmospheric phenomena without the use of fine-scale grids. These parameterizations, however, may vary significantly in their utility, and are often underconstrained and therefore somewhat heuristic. Furthermore, models are often highly sensitive to the particular parameterizations used (see e.g. Slingo et al. 1994; Villafuerte et al. 2021), indicating that a more universal approach to developing convective paratemerizations would be beneficial. In this paper, we investigate the effect of a small-scale nonlinear convective cloud field on the propagation of large-scale waves through a stratified atmosphere, using a systematic multiple-scales approach. In particular, we motivate (within a simplified setting) a method by which a convective parameterization may be closed in a manner which is fully consistent with the governing fluid dynamical equations. This contrasts with classical mass-flux convective parameterization schemes (e.g. Ooyama 1971; Arakawa and Schubert 1974; Gregory and Rowntree 1990; Emanuel 1991; Gregory 2002) in which the unresolved fluxes are constructed using physically motivated heuristics.

A formal framework for a multiple-scales asymptotic approach to the interaction between long waves and convection has been developed by Majda and Klein (2003); Biello and Majda (2005, 2010), with a particular focus on understanding the dynamics of the Madden-Julian oscillation and tropical intraseasonal behaviour in general. The outcome of these studies is a hierarchy of equation sets which apply on different horizontal scales, with the largest scale equations being coupled to the smaller-scale equations through averaged buoyancy and momentum flux terms which must be resolved to close the system. The homogenization framework to be employed in the present work provides an example of an explicit closure, by showing how the flux terms in the largest scale equations can be calculated explicitly from the large-scale variables, at the cost of making simplifying assumptions about the nature of the small-scale flow. Specifically, here we focus on the interaction between long waves and a field of localized convective cells (with horizontal scale $\lesssim$ 10km) representing cumulus clouds. These axisymmetric 'cloud-like' circulations are steady solutions to the full nonlinear, non-hydrostatic Boussinesq equations driven by a steady axisymmetric localized heating. Similar (but larger-scale) axisymmetric flows in the atmosphere have been studied by Wirth (1998); Wirth and Dunkerton (2006); Plumb and Hou (1992) as models for for the development of monsoons and hurricanes. It is to be emphasized that the cloud circulations we investigate are strongly nonlinear, and that the homogenization method does not depend upon linearizing their interaction with the large-scale flow. It should also be noted that the restriction to a field of steady identical clouds can be relaxed, and considerably more realistic scenarios can be addressed using the same method, at the expense of additional complexity.

The method of homogenization was developed initially to understand the properties of composite media (e.g. Rayleigh 1892), and has found multiple previous applications in geophysical fluid dynamics, most notably in the study of flows over small-scale topgraphy (e.g. Vanneste 2000a,b, 2003; Benilov 2000; Li and Mei 2014; Goldsmith and Esler 2021; Radko 2022a,b). Analogously to the present study, the strength of the method is that it allows the effect of *nonlinear* topographic variations to be modelled accurately. For simplicity, most of the studies above focussed on applying the method to the linearized large-scale equations, and major results included, for example, the corrections to Rossby and gravity wave dispersion relations due to the topographic variations. Notable exceptions are the paper by Vanneste (2003), and the recent work of Radko (2022a,b) where the homogenization method is successfully applied to the full nonlinear quasi-geostrophic shallow water (one and two-layer) equations, illustrating the potential for the full parameterization of small-scale effects in large-scale equations.

In common with most of the works listed above, the present study will, as a first step, focus on a linear system, namely the linearized stratified Boussinesq equations in a mid-latitude β-channel. Note, however, that the system will be linearized about a basic state which includes the nonlinear cloud circulations. It is well-known that in the absence of clouds, modal decomposition in the vertical (see e.g. Gill 1982, §6.11; Olbers et al. 2012, Ch. 8) can be used to separate disturbances into individual modes (barotropic, first baroclinic, second baroclinic etc.), for each of which the horizontal structure is governed by the shallow water equations with a mode-dependent wave speed. It will be shown below that the effect of the cloud field is to couple these wave modes to one another.

A similar coupling of wave modes is known to occur when waves propagate over slowly varying topography (Craig 1987; Smith and Young 2002; Kelly et al. 2010; Kelly 2016; Garrett and Kunze 2007). For example, in the oceanic context the interaction between a gently sloping seabed and surface waves can act to excite internal waves within the fluid. Here, the coupling is manifest through additional terms in the equations, which have the form of non-local integral operators that in their discretized form are known as *transilient matrices* (Stull 1984; Romps and Kuang 2011). Originating in turbulence theory, transilient matrices are used to model the non-local vertical redistribution of conserved quantities due to the rapid turbulent rearrangement of fluid parcels in convective columns (see e.g. Cheng et al. 2017). Here, the analogous integral operators model a continuous-in-time, non-local, vertical rearrangement of horizontal momentum and buoyancy. One of the main outcomes of this work is a method by which the kernels of the integral operators (here referred to as 'transilient kernels') can be explicitly diagnosed for any given cloud field. In future it is hoped that these results could be adapted for use in numerical weather simulations - an area of research where the utility of transilient operators as a means of parameterizing turbulence and convection is already being realized (see e.g. Forster et al. 2007; Kuell and Bott 2022).

To allow for a straightforward presentation of the key concepts and main qualitative results, a number of simplifying assumptions are made. In particular, the clouds are assumed to be sufficiently well-separated so that the circulations due to each individual cloud, despite being strongly nonlinear in the cloud core region, interact only linearly where they overlap. For simplicity, the cloud circulations are driven by imposed steady heating fields, which represent the release of latent heat by condensation in cumulus cloud updrafts. Including time dependence in the cloud circulation, which is obviously necessary when considering the relevant timescales, is postponed to a future study. Another simplifying assumption with this approach is that effects due to a dynamically active moisture field will be of secondary importance. Despite this, a suitable choice of heating can result in a plausible cloud circulation with a strong, narrow updraft region surrounded by a wide region of subsidence. The above two assumptions should be viewed as the weakest points in our model from a physical standpoint; however, they act as a good starting point upon which to build our asymptotic theory, and the development of models which relax these assumptions is left as a topic for future study.

The structure of this paper is as follows. In section 2 we derive the equations governing long wave propagation in the presence of a cloud field in an incompressible, stratified atmosphere via the method of homogenization. In particular, we derive three systems of equations - those governing the nonlinear cloud circulation, the large-scale averaged equations, and the so-called 'cell problem' which couples the cloud circulation to the large-scales. The central result of this paper, namely the homogenized integro-differential equations are presented here, with convection shown to enter the dynamics through terms involving integral operators which are non-local in the vertical direction. In section 3, we give a detailed description of how the transilient kernels derived in the previous section may be diagnosed for a particular cloud field. This involves a review of wave mode decomposition in the absence of convection, followed by its extension to our problem. We then detail the numerical methods by which the cloud circulation problem and the cell problems associated with homogenization are solved. Finally, in section 4, properties of the homogenized equations are discussed, with a particular emphasis on how convection affects the dispersive characteristics of waves in a mid-latitude β–channel. Conclusions are drawn in section 5.

2. Homogenization of the Boussinesq Equations

The starting point for our analysis is the nonlinear, non-hydrostatic Boussinesq equations in a β–channel

$$\partial_t \mathbf{v} + f\mathbf{k}\times\mathbf{v} + (\mathbf{v}\cdot\nabla)\,\mathbf{v} = -\nabla p + b\mathbf{k} + \nabla\cdot(\nu\nabla\mathbf{v}), \tag{1a}$$

$$\nabla\cdot\mathbf{v} = 0, \tag{1b}$$

$$\partial_t b + (\mathbf{v}\cdot\nabla)\,b + N^2 w = Q + \nabla\cdot(\kappa\nabla b). \tag{1c}$$

Here $\mathbf{v} = (u, v, w)^T$ is the velocity field, b is the buoyancy, p is the perturbation pressure field, $f = f_0 + \beta Y$ is the Coriolis parameter and N is the buoyancy frequency. The final terms in equations (1a) and (1c) parameterize the turbulent diffusion of momentum and buoyancy with an eddy viscosity ν and diffusivity κ respectively. The quantity Q is a diabatic heat source parameterizing latent heat release as moisture in the atmosphere condenses (see e.g. Ogura and Phillips 1962; Ling and Zhang 2013; Holton and Hakim 2013, Ch. 11). To motivate the scaling analysis to follow, in which lower case variables will denote the natural length scales for the averaged equations and upper case variables the shorter horizontal scales associated with the clouds, the isotropic spatial coordinate system is here denoted (X,Y,z) with the associated gradient operator being $\nabla = (\partial_X, \partial_Y, \partial_z)^T$.

Since we are ultimately concerned with long wave propagation in the presence of steady, cumulus convection, it is helpful to non-dimensionalize (1a–1c) on the scale of an individual cloud. Assuming that the height and horizontal extent of the circulation associated with a cumulus cloud are of the same order, we take the tropopause height H as a typical length scale. We then have NH as the velocity scale, N^2H^2 as the perturbation pressure scale, and N^2H as the buoyancy scale. Correspondingly, the eddy viscosity ν and diffusivity κ are both scaled as NH^2, and the diabatic heat source is scaled as N^3H. The time scale associated with t is chosen to be f_0^{-1} (which is indeed much greater than the time scale N^{-1}) so that the temporal variability is found only on the scale of the long waves. Consequently, the equations may be written in non-dimensional form as

$$\varepsilon\left(\partial_t \mathbf{v} + f\mathbf{k}\times\mathbf{v}\right) + (\mathbf{v}\cdot\nabla)\,\mathbf{v} = -\nabla p + b\mathbf{k} + \nabla\cdot(\nu\nabla\mathbf{v}), \tag{2a}$$

$$\nabla\cdot\mathbf{v} = 0, \tag{2b}$$

$$\varepsilon\partial_t b + (\mathbf{v}\cdot\nabla)\,b + w = Q + \nabla\cdot(\kappa\nabla b), \tag{2c}$$

where variable names are retained for the non-dimensional quantities, and where $\varepsilon = f_0/N$. In this case, the non-dimensional Coriolis parameter becomes $f = 1 + \varepsilon\bar{\beta}Y$ where $\bar{\beta} = \beta L_R/f_0$ is the rescaled beta parameter, with $L_R = NH/f_0$ being the Rossby radius of deformation appropriate to the mid-latitude atmosphere. Using typical values of the buoyancy frequency and Coriolis parameter for the mid-latitude troposphere ($N = 10^{-2}\mathrm{s}^{-1}$, $f_0 = 10^{-4}\mathrm{s}^{-1}$) results in a value of $\varepsilon \approx 0.01$.

We are interested in the propagation of long waves in (2a–2c) through a steady background flow $\{\overline{\mathbf{v}}, \overline{p}, \overline{b}\}$. This steady flow is defined as the leading-order solution to (2a–2c) in the presence of a specified heating Q which determines the cloud field. We also wish to direct our focus towards arrays of weakly-interacting clouds - that is to say that the clouds must be separated by a great enough distance that their interactions have a negligible effect on the dynamics. Under such assumptions, the diabatic heating may be expressed as a linear combination of the contributions from each individual source centred at $(X^{(i)}, Y^{(i)})$ as

$$Q = \sum_{i=1}^{\infty} Q_0(r^{(i)}, z), \tag{3}$$

where $r^{(i)} \equiv |\mathbf{X} - \mathbf{X}^{(i)}| = \sqrt{(X - X^{(i)})^2 + (Y - Y^{(i)})^2}$. In the above decomposition and from here onwards, variables subscripted with a 0 indicate the contribution from a single cloud centred at the origin. It is assumed that the response to the heating may be decomposed in a similar fashion, as

$$\overline{\mathbf{v}} = \sum_{i=1}^{\infty} \overline{\mathbf{v}}_0(r^{(i)}, z), \qquad \overline{p} = \sum_{i=1}^{\infty} \overline{p}_0(r^{(i)}, z), \tag{4a,b}$$

$$\overline{b} = \sum_{i=1}^{\infty} \overline{b}_0(r^{(i)}, z). \tag{4c}$$

Finally, in part as a mathematical device to be used to simplify aspects of the the analysis below, albeit one that has a reasonable physical basis since turbulence can be expected to be strongest in the vicinity of the clouds, both ν and κ are taken to vary with distance from the cloud core, taking the form

$$\nu = \sum_{i=1}^{\infty} \nu_0(r^{(i)}), \qquad \kappa = \sum_{i=1}^{\infty} \kappa_0(r^{(i)}). \tag{5a,b}$$

This is a reasonable assumption from a physical standpoint, since the effects of turbulence are minimal outside of the atmospheric boundary layer, except for in regions of high convective activity (Holtslag 2003). The background flow is therefore found from the steady 'cloud circulation problem' (CCP hereafter), given by

$$(\overline{\mathbf{v}}_0 \cdot \nabla)\, \overline{\mathbf{v}}_0 = -\nabla \overline{p}_0 + \overline{b}_0 \mathbf{k} + \nabla \cdot (\nu_0 \nabla \overline{\mathbf{v}}_0)\,, \tag{6a}$$

$$\nabla \cdot \overline{\mathbf{v}}_0 = 0, \tag{6b}$$

$$(\overline{\mathbf{v}}_0 \cdot \nabla)\, \overline{b}_0 + \overline{w}_0 = Q_0 + \nabla \cdot (\kappa_0 \nabla \overline{b}_0), \tag{6c}$$

where the single source $Q_0 = Q_0(r, z)$ is centred on the origin. Consequently the solutions to the CCP (6a–6c) are axisymmetric functions, i.e. $\{\overline{\mathbf{v}}_0, \overline{p}_0, \overline{b}_0\} = \{\overline{\mathbf{v}}_0(r,z), \overline{p}_0(r,z), \overline{b}_0(r,z)\}$. Note that the assumption of well-separated clouds is analogous to an assumption of well-separated seamounts that has been widely applied in the corresponding flow over topography problem (Benilov 2000; Vanneste 2000b; Goldsmith and Esler 2021).

Here we are interested in linear waves with horizontal wavelengths at the order of the Rossby radius L_R propagating on the background flow. Therefore, in order to examine interactions across spatial scales, we introduce the large, horizontal spatial variable $\mathbf{x} = \varepsilon \mathbf{X}$, with $\mathbf{x} = (x, y, 0)^T$ and expand the gradient operator according to the multiple-scales formalism as

$$\nabla \longrightarrow \varepsilon \nabla_{\mathbf{x}} + \nabla, \tag{7}$$

where $\nabla_{\mathbf{x}} = (\partial_x, \partial_y, 0)^T$. In conjunction with this, we introduce a horizontal averaging operator over the small scales $\langle \cdot \rangle$ as is typical in the method of homogenization. For a function $g(\mathbf{X})$ which may be decomposed as in (3), this operator acts as

$$\begin{aligned} \langle g \rangle &= \frac{1}{|\Omega|} \int_\Omega g(\mathbf{X}) \, \mathrm{d}\mathbf{X} \\ &= \frac{1}{|\Omega|} \int_\Omega \sum_{i=1}^{\infty} g_0(|\mathbf{X} - \mathbf{X}^{(i)}|, \theta) \, \mathrm{d}\mathbf{X} \\ &= \overline{n} \langle g_0 \rangle_0, \end{aligned} \tag{8}$$

where

$$\langle g_0 \rangle_0 = \int_0^{2\pi} \int_0^{\infty} g_0(r, \theta) \, r \mathrm{d}r \mathrm{d}\theta, \tag{9}$$

and $\overline{n}$ is the number density of clouds per unit area in Ω. It turns out that the interesting, tractable regime occurs when the number density of clouds is $O(\varepsilon)$, hence we write $\overline{n} = \varepsilon n$ where n is of order unity. Linearizing about the background flow by writing

$$\mathbf{v} \longrightarrow \overline{\mathbf{v}} + \delta \mathbf{v}, \quad p \longrightarrow \overline{p} + \delta p, \quad b \longrightarrow \overline{b} + \delta b,$$

where $\delta \ll \varepsilon \ll 1$, then inserting (7) into (2a–2c), and retaining only terms at leading order in δ gives

$$\varepsilon\left[\partial_t \mathbf{v} + f\mathbf{k}\times\mathbf{v} + (\overline{\mathbf{v}}\cdot\nabla_{\mathbf{x}})\,\mathbf{v}\right] + (\overline{\mathbf{v}}\cdot\nabla)\,\mathbf{v} + (\mathbf{v}\cdot\nabla)\,\overline{\mathbf{v}} = -\varepsilon\nabla_{\mathbf{x}}p - \nabla p + b\mathbf{k} \qquad (10a)$$
$$+\varepsilon^2\nu\nabla_{\mathbf{x}}^2\mathbf{v} + \varepsilon\nu\nabla_{\mathbf{x}}\cdot\nabla\mathbf{v} + \varepsilon\nabla\cdot(\nu\nabla_{\mathbf{x}}\mathbf{v}) + \nabla\cdot(\nu\nabla\mathbf{v})$$

$$\varepsilon\nabla_{\mathbf{x}}\cdot\mathbf{v} + \nabla\cdot\mathbf{v} = 0, \qquad (10b)$$

$$\varepsilon\left[\partial_t b + (\overline{\mathbf{v}}\cdot\nabla_{\mathbf{x}})\,b\right] + (\overline{\mathbf{v}}\cdot\nabla)\,b + (\mathbf{v}\cdot\nabla)\,\overline{b} + w = \varepsilon^2\kappa\nabla_{\mathbf{x}}^2 b + \varepsilon\kappa\nabla_{\mathbf{x}}\cdot\nabla b + \varepsilon\nabla\cdot(\kappa\nabla_{\mathbf{x}}b) + \nabla\cdot(\kappa\nabla b)\,. \qquad (10c)$$

where the unbarred variables now refer to perturbations from the (barred) basic state which includes the clouds.

Next, the time dependent, unbarred variables in (10a–10c) are decomposed into their averaged parts (denoted by capitals) using the averaging operator (8), and fluctuations (denoted with tildes), by writing

$$\mathbf{v} = \mathbf{U}(\mathbf{x},z,t) + \varepsilon W(\mathbf{x},z,t)\mathbf{k} + \tilde{\mathbf{v}}(\mathbf{x},\mathbf{X},z,t), \qquad (11a)$$

$$p = P(\mathbf{x},z,t) + \tilde{p}(\mathbf{x},\mathbf{X},z,t), \qquad (11b)$$

$$b = B(\mathbf{x},z,t) + \tilde{b}(\mathbf{x},\mathbf{X},z,t). \qquad (11c)$$

The hydrostatic approximation is made implicitly here, because the averaged vertical velocity vanishes at leading order and correspondingly $\mathbf{U} = (U,V,0)^T$ denotes the averaged horizontal components of velocity. The fluctuating components in the above expansions must all have zero horizontal average, i.e. $\langle\tilde{\mathbf{v}}\rangle = 0$ and $\langle\tilde{p}\rangle = \langle\tilde{b}\rangle = 0$.

Inserting (11a–11c) into equations (10a–10c) and applying the averaging operator, we find at leading order

$$\partial_t\mathbf{U} + f\mathbf{k}\times\mathbf{U} + n\partial_z\left\langle\overline{w}_0\tilde{\mathbf{u}}_0 + \tilde{w}_0\overline{\mathbf{u}}_0\right\rangle_0 = -\nabla_{\mathbf{x}}P + \mathbf{S}_{\nu_0}, \qquad (12a)$$

$$\partial_z P = B, \qquad (12b)$$

$$\nabla_{\mathbf{x}}\cdot\mathbf{U} + \partial_z W = 0, \qquad (12c)$$

$$\partial_t B + n\partial_z\langle\overline{w}_0\tilde{b}_0 + \tilde{w}_0\overline{b}_0\rangle_0 + W = S_{\kappa_0}, \qquad (12d)$$

where

$$\mathbf{S}_{\nu_0} = n\langle \nu_0\rangle_0 \partial^2_{zz}\mathbf{U} + n\partial_z\langle \nu_0 \nabla \tilde{\mathbf{u}}_0\rangle_0, \tag{13a}$$

$$S_{\kappa_0} = n\langle \kappa_0\rangle_0 \partial^2_{zz}B + n\partial_z\langle \kappa_0 \nabla \tilde{b}_0\rangle_0. \tag{13b}$$

Equations (12a–12d) are simply the linearized, hydrostatic Boussinesq equations with additional terms involving the background cloud circulations (barred variables) and the perturbations induced by their interaction with the mean flow (tilde variables). These additional terms are the divergences of the vertical fluxes of horizontal momentum and buoyancy due to the presence of the clouds. Additionally, there are terms associated with the averaged eddy viscosity $\mathbf{S}_{\nu_0}$ and diffusivity S_{κ_0} due to turbulence in the clouds. For these terms to formally enter at the correct order, it is necessary to assume that the profiles of eddy viscosity and diffusivity $\nu_0(r)$ and $\kappa_0(r)$ remain of order unity only in the vicinity of the clouds, so that the integrals in (9) remain bounded. (In fact, when we come to consider the averaged equations below, we will assume that ν and κ are sufficiently small that $\mathbf{S}_{\nu_0}$ and S_{κ_0} can be neglected altogether.)

The leading order part of equations (10a–10c), after insertion of the expansion (11a-11c), is a linear equation in the perturbation quantities $\{\tilde{\mathbf{v}}, \tilde{p}, \tilde{b}\}$. Just as for the CCP above, this equation can be decomposed into contributions from individual clouds, and it is therefore necessary to consider only the single-cloud problem in $\{\tilde{\mathbf{v}}_0, \tilde{p}_0, \tilde{b}_0\}$ given by

$$(\overline{\mathbf{v}}_0\cdot\nabla)\,\tilde{\mathbf{v}}_0 + (\tilde{\mathbf{v}}_0\cdot\nabla)\,\overline{\mathbf{v}}_0 + \nabla\tilde{p}_0 - \tilde{b}_0\mathbf{k} - \nabla\cdot(\nu_0\nabla\tilde{\mathbf{v}}_0) = -(\mathbf{U}\cdot\nabla)\,\overline{\mathbf{v}}_0 - \overline{w}_0\partial_z\mathbf{U} + \mathbf{s}_{\nu_0}, \tag{14a}$$

$$\nabla\cdot\tilde{\mathbf{v}}_0 = 0, \tag{14b}$$

$$(\overline{\mathbf{v}}_0\cdot\nabla)\,\tilde{b}_0 + (\tilde{\mathbf{v}}_0\cdot\nabla)\,\overline{b}_0 + \tilde{w}_0 - \nabla\cdot\left(\kappa_0\nabla\tilde{b}_0\right) = -(\mathbf{U}\cdot\nabla)\,\overline{b}_0 - \overline{w}_0\partial_z B + s_{\kappa_0}, \tag{14c}$$

where $\mathbf{s}_{\nu_0} = \nu_0\partial^2_{zz}\mathbf{U}$, $s_{\kappa_0} = \kappa_0\partial^2_{zz}B$ and here $\{\overline{\mathbf{v}}_0, \overline{b}_0\}$ are the solutions of the CCP (6a-6c). Equations (14a–14c) will be referred to as the ‘linear cell problem equations’ (LCPE hereafter). It constitutes a linear, elliptic system of partial differential equations which can be solved to find $\{\tilde{\mathbf{v}}_0, \tilde{p}_0, \tilde{b}_0\}$ in terms of the averaged horizontal velocity and buoyancy fields $\{\mathbf{U}, B\}$. In fact, since (14a–14c) is also linear in $\mathbf{U}$ and B, the solution establishes a linear relationship between $\{\tilde{\mathbf{v}}_0, \tilde{p}_0, \tilde{b}_0\}$ and {U,B} which is the key to deriving the homogenized equations describing the large-scale dynamics. Note, however, that the nature of this linear relationship has a *nonlinear* dependence on the details of the cloud circulations described by the CCP solution $\{\overline{\mathbf{v}}_0, \overline{b}_0\}$.

In the low diffusivity limit of interest (ν_0, $\kappa_0 \to 0$) the diffusive terms on the left-hand side must be retained in order that the solution of the LCPE remains regular, while $\mathbf{s}_{\nu_0}, s_{\kappa_0}$ can be neglected because they are small compared with the other terms on the right-hand side. In the next section it will be shown that, in this limit, the linear relationship established between $\{\tilde{\mathbf{v}}_0, \tilde{p}_0, \tilde{b}_0\}$ and $\{\mathbf{U}, B\}$ allows the momentum and heat flux terms appearing in (12a–12d) to be expressed as

$$\langle \overline{w}_0 \tilde{\mathbf{u}}_0 + \tilde{w}_0 \overline{\mathbf{u}}_0 \rangle_0 = \mathcal{K}_1 \mathbf{U} + \mathcal{K}_2 \partial_z \mathbf{U}, \tag{15a}$$

$$\langle \overline{w}_0 \tilde{b}_0 + \tilde{w}_0 \overline{b}_0 \rangle_0 = \mathcal{L} \partial_z B, \tag{15b}$$

where the linear operators $\mathcal{K}_1$, $\mathcal{K}_2$ and $\mathcal{L}$ act on functions $G(z)$ defined in the vertical as

$$\mathcal{K}_1 G = \int_0^1 K_1(z,z') G(z')\, \mathrm{d}z', \tag{16a}$$

$$\mathcal{K}_2 G = \int_0^1 K_2(z,z') G(z')\, \mathrm{d}z', \tag{16b}$$

$$\mathcal{L} G = \int_0^1 L(z,z') G(z')\, \mathrm{d}z'. \tag{16c}$$

The integral kernels $K_1(z,z')$, $K_2(z,z')$ and $L(z,z')$ will be referred to as 'transilient kernels' hereafter because they are continuous analogues of the transilient matrix, a concept which has its origin in the theory of convective turbulence (Stull 1984; Romps and Kuang 2011; Bhamidipati et al. 2020; Cheng et al. 2017). Below K_1, K_2 and L will be shown to be smooth functions which depend upon the details of the CCP solutions $\{\overline{\mathbf{v}}_0, \overline{b}_0\}$. Physically, the non-local action of the integral operators quantifies the process of the near-instantaneous rearrangement of fluid particles in the vertical, by turbulent updrafts and downdrafts with small horizontal scale.

Inserting the expressions (15a-15b) for the vertical fluxes into the averaged equations (12a–12d) results in the *homogenized equations*

$$\partial_t \mathbf{U} + f\mathbf{k}\times\mathbf{U} + n\partial_z\left(\mathcal{K}_1\mathbf{U}\right) = -\nabla_{\mathbf{x}}P + n\partial_z\left(\mathcal{K}_2\partial_z\mathbf{U}\right), \tag{17a}$$

$$\partial_z P = B, \tag{17b}$$

$$\nabla_{\mathbf{x}}\cdot\mathbf{U} + \partial_z W = 0, \tag{17c}$$

$$\partial_t B + W = n\partial_z\left(\mathcal{L}\partial_z B\right), \tag{17d}$$

Equations (17a-17d) are the main result of this work, and govern the propagation of linear disturbances through the atmosphere in the presence of the cloud circulations. They are solved with the rigid lid boundary conditions

$$\partial_z\mathbf{U} = 0, \quad W = B = 0, \quad \text{on} \quad z = 0, 1. \tag{18}$$

The details of how to solve the cloud circulation problem (CCP), the linear cell problem equations (LCPE) and thus obtain the transilient kernels, will be given the next section. Readers who are not interested in these technicalities can skip forwards to section 4 where the properties and physical behaviour of (17a-17d) are discussed.

3. Solution of the CCP, LCPE and calculation of the transilient kernels

The aim of this section is to establish the linear relationship between the large-scale flow and the small-scale vertical fluxes of horizontal momentum and buoyancy given by (15a-15b), and then to demonstrate how the transilient kernels K_1, K_2 and L appearing in the homogenized equations may be calculated. The starting point is simply to specify a heating profile $Q_0(r,z)$ which drives the individual cloud circulations in the CCP. Then

(a) A numerical method for solving the CCP to obtain the cloud circulation variables $\{\overline{\mathbf{v}}_0, \overline{b}_0\}$ is described and example solutions are calculated.

(b) The vertical mode decomposition used for the solution of the LCPE is described.

(c) The decomposition of the LCPE into a set of 'kernel cell problems' is detailed.

(d) The numerical solution of the kernel cell problems and therefore the LCPE are described.

(e) Example calculations of the transilient kernels are presented.

a. Solution of the CCP

In solving the CCP (6a–6c) to obtain the circulation variables $\{\overline{\mathbf{v}}_0, \overline{b}_0\}$, the first step is to specify a suitable heating profile $Q_0(r,z)$ in order to drive the cumulus cloud-like circulations. For the numerical solutions below, constant diffusivities $\nu_0 = \kappa_0 = 0.05$ are set within the computational domain, which for numerical convenience is truncated at an outer boundary $r = r_{\text{out}}$ where a free-slip boundary condition is applied. Tests have confirmed that for the choice made below ($r_{\text{out}} = 5$) the outer boundary is sufficiently distant for it to have minimal impact on the CCP solutions (see appendix D). Note that, for consistency with the analysis above, there is an implicit assumption that ν_0 and κ_0 both decay to zero (or formally, are of order ε) in between clouds, as is physically consistent with higher eddy diffusivities within regions of the convective activity.

Since the CCP is axisymmetric, the components of the velocity vector are independent of the azimuthal coordinate θ, and the azimuthal component of velocity is zero. The background flow can therefore be expressed as

$$\overline{\mathbf{v}}_0 = \overline{u}_0^r(r,z)\mathbf{e}_r + \overline{w}_0(r,z)\mathbf{k}, \tag{19}$$

where $\overline{u}_0^r$ is the radial component of velocity, and $\mathbf{e}_r$ and $\mathbf{k}$ are the cylindrical polar coordinate basis vectors in the radial and vertical directions respectively. Since the flow is incompressible, a streamfunction $\overline{\psi}_0$ can be introduced from which the velocity can be calculated according to

$$\overline{u}_0^r = -\frac{1}{r}\partial_z\overline{\psi}_0, \quad \overline{w}_0 = \frac{1}{r}\partial_r\overline{\psi}_0, \tag{20}$$

and the continuity equation (6b) is thus automatically satisfied. Note that we retain the overline and subscript 0 notation here for clarity when referring to solutions of the CCP. Introducing the azimuthal component of vorticity $\overline{\zeta}_0$ which is defined as

$$\overline{\zeta}_0 = \partial_r\overline{w}_0 - \partial_z\overline{u}_0^r, \tag{21}$$

the CCP can be expressed in streamfunction-vorticity form as

$$\mathcal{J}\left(\overline{\psi}_0, \overline{\zeta}_0/r\right) - \partial_r \overline{b}_0 = \nu_0 \left(\nabla^2 \overline{\zeta}_0 - \frac{\overline{\zeta}_0}{r^2}\right), \tag{22a}$$

$$\frac{1}{r}\left(\partial^2_{rr}\overline{\psi}_0 - \frac{1}{r}\partial_r \overline{\psi}_0 + \partial^2_{zz}\overline{\psi}_0\right) = \overline{\zeta}_0, \tag{22b}$$

$$\frac{1}{r}\mathcal{J}\left(\overline{\psi}_0, \overline{b}_0\right) + \frac{1}{r}\partial_r \overline{\psi}_0 = Q_0 + \kappa_0 \nabla^2 \overline{b}_0, \tag{22c}$$

where $\mathcal{J}$ is the usual Jacobian operator. Equations (22a-22c) constitute a nonlinear system of equations in the three variables $\overline{\psi}_0, \overline{\zeta}_0, \overline{b}_0$ to be solved in the numerical domain $(r, z) \in (0, r_{\text{out}}) \times (0, 1)$. A rigid lid boundary is imposed at $z = 1$. The associated boundary conditions are

$$\overline{\psi}_0 = \overline{\zeta}_0 = \overline{b}_0 = 0, \quad \text{on} \quad z = 0, 1, \tag{23a}$$

$$\overline{\psi}_0 = \overline{\zeta}_0 = \partial_r \overline{b}_0 = 0, \quad \text{on} \quad r = 0, \tag{23b}$$

$$\overline{\psi}_0 = \overline{\zeta}_0 = \overline{b}_0 = 0, \quad \text{on} \quad r = r_{\text{out}}. \tag{23c}$$

In order that a steady solution can be found the heating profile Q_0 should be chosen to have zero integral over the domain,

$$\int_0^1 \int_0^{r_{\text{out}}} Q_0 \, r \mathrm{d}r \mathrm{d}z = 0, \tag{24}$$

so that there is no net source of total buoyancy in the system.

Fig. 1 shows numerical solutions of (22a–22c) subject to (23a–23c) for the diabatic heat source given by

$$Q_0(r, z) = 12\mathrm{e}^{-5(r^2+z)}(1 - 5r^2)\sqrt{z(1-z)}. \tag{25}$$

The nonlinear iterative algorithm used to obtain the solution is described in appendix A. The illustrated solution captures the basic features of the circulation surrounding a cumulus cloud - that is, the circulation occupies the full height of the troposphere, with a narrow, localized updraft region at $r = 0$, and a much broader and less intense subsidence away from the cloud core. For typical values of the dimensional buoyancy frequency $N = 0.01\text{s}^{-1}$, and tropopause height $H = 10^4$m, the maximum horizontal and vertical velocities of the fluid are approximately $w_{\max} \approx 10\text{ms}^{-1}$ and $u_{\max} \approx 5\text{ms}^{-1}$, broadly consistent with measurements of cumulus convection. The buoyancy

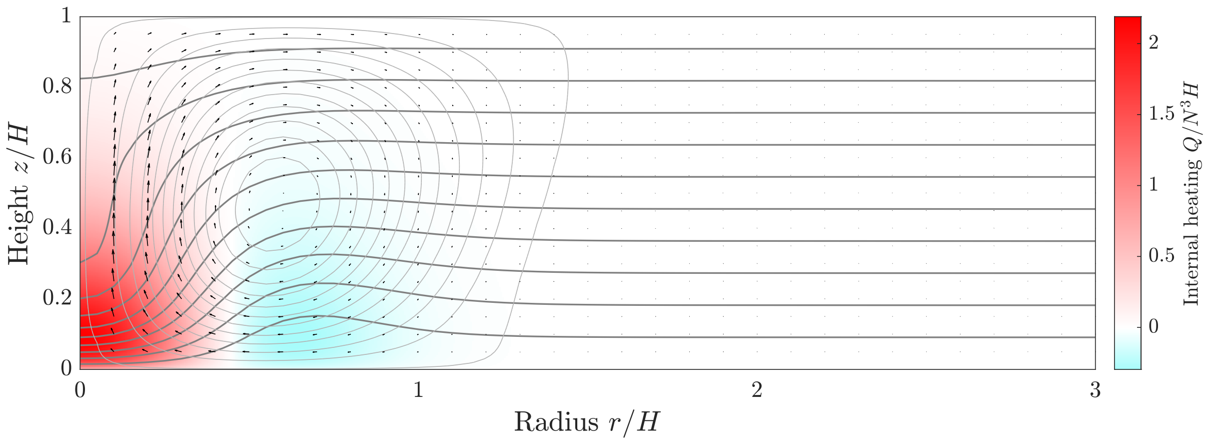

FIG. 1. Numerical solutions to (22a–22c) for the specified heat distribution given in (25) and $\nu_0 = \kappa_0 = 0.05$. The streamlines of $\overline{\psi}_0$ are shown as closed, grey curves, and the contours of the total buoyancy $b_{\text{tot}} = \overline{b}_0 + z$ are shown as black curves. The heat distribution is shown using color, with red and blue representing regions of heating and cooling respectively. Arrows are included to indicate the direction of cloud circulation.

perturbations are localized near to the heat source, and have a maximum dimensional value of approximately 0.65ms^{-2}. Note also that using the maximum horizontal velocity as a reference, and recalling that the local horizontal scale of motion in the cloud is given by $L_c = H \approx 10^4$m, the local Rossby number is given by $\text{Ro} = u_{\max}/L_c f_0 \approx 5$, justifying the omission of rotation terms in the CCP equations.

A necessary condition for the solution of the CCP to be convectively stable to small perturbations is that the vertical gradient in total buoyancy, which in non-dimensional form is

$$N^2_{\text{tot}}(r,z) \equiv \partial_z b_{\text{tot}}(r,z) = 1 + \partial_z \overline{b}_0(r,z), \tag{26}$$

must be everywhere positive. Additionally, a physical feature of deep convection that we would like our CCP solution to reproduce, is that the vertical gradient in the total buoyancy is significantly reduced in the cloud core compared with the background atmosphere. The structure of N^2_{tot} is shown in Fig. 2, and it is seen that the total stratification does indeed remain positive everywhere, and is reduced by an order of magnitude within the cloud core compared to its background value.

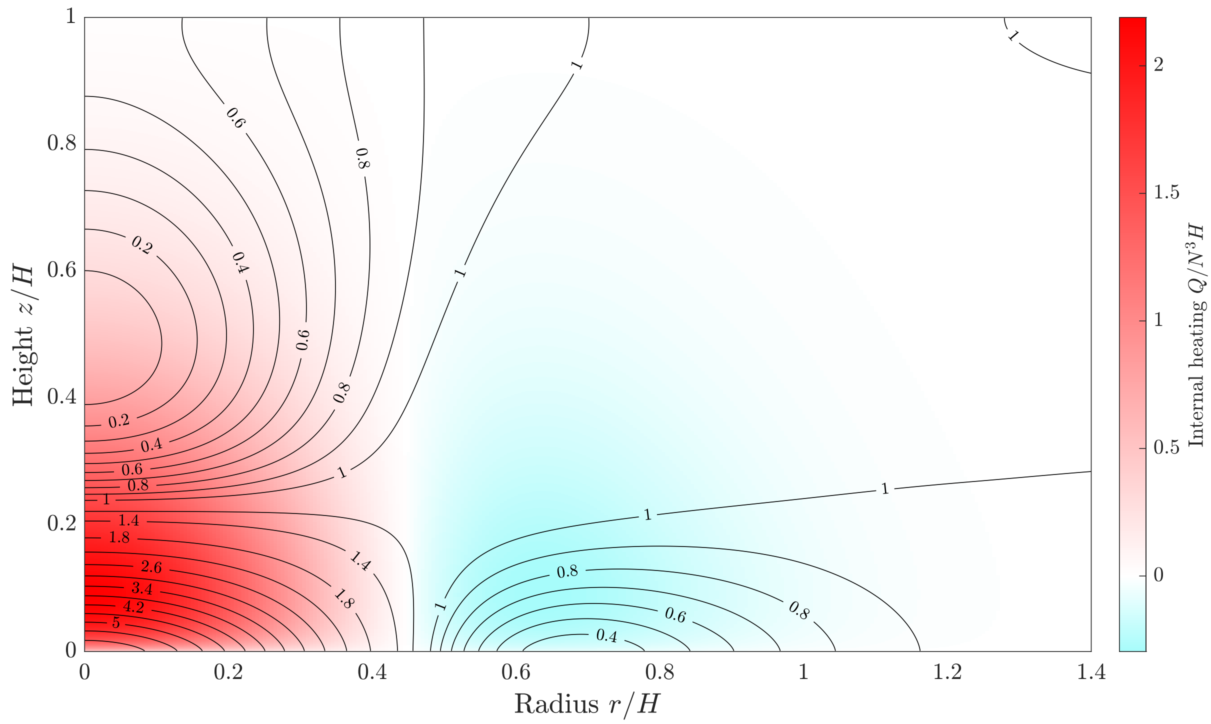

FIG. 2. Contours of $N_{\text{tot}}^2(r,z)$ for the circulation driven by the heating profile (25).

b. Vertical mode decomposition

The first key step in our solution of the LCPE (14a–14c) is to establish a set of vertical modes onto which our solutions can be projected. The approach to be taken is the standard one used for e.g. the Matsuno-Gill model (Matsuno 1966; Gill 1980) and is discussed in e.g Gill (1980, §6.11) and Olbers et al. (2012, Ch. 8). Following (Kelly 2016), the vertical modes in question satisfy

$$[\mathbf{U}, P](\mathbf{x}, z, t) = \sum_{j=0}^{\infty} \left[\tilde{\mathbf{U}}_j, \tilde{P}_j\right](\mathbf{x}, t)\phi_j(z), \tag{27a}$$

$$[W, B](\mathbf{x}, z, t) = \sum_{j=0}^{\infty} \left[\tilde{W}_j, \tilde{B}_j\right](\mathbf{x}, t)\Phi_j(z), \tag{27b}$$

where the baroclinic modes $j = 1, 2, 3, \ldots$ have structure

$$\phi_j(z) = \sqrt{2}\cos(j\pi z), \qquad \Phi_j(z) = \frac{\sqrt{2}}{j\pi}\sin(j\pi z), \tag{28a}$$

and the barotropic mode $j = 0$ has $\phi_0(z) = 1$, $\Phi_0(z) = 0$.

The orthogonality results

$$\int_0^1 \phi_j(z)\phi_k(z)\,\mathrm{d}z = \delta_{jk}, \tag{29}$$

$$\int_0^1 \Phi_j(z)\Phi_k(z)\,\mathrm{d}z = c_j c_k \delta_{jk}, \tag{30}$$

allow for straightforward calculation of the the coefficients in (27a-27b),

$$\left[\tilde{W}_j, \tilde{B}_j\right](\mathbf{x},t) = \frac{1}{c_j^2}\int_0^1 \left[W,B\right](\mathbf{x},z',t)\,\Phi_j(z')\,\mathrm{d}z', \tag{31}$$

$$\left[\tilde{\mathbf{U}}_j, \tilde{P}_j\right](\mathbf{x},t) = \int_0^1 [\mathbf{U},P](\mathbf{x},z',t)\,\phi_j(z')\,\mathrm{d}z'. \tag{32}$$

It is well known that under such a decomposition the Boussinesq equations (i.e. equations (17a-17d) with zero cloud number density, $n = 0$) reduce to a sequence of linear shallow water equations

$$\partial_t \tilde{\mathbf{U}}_j + f\mathbf{k}\times\tilde{\mathbf{U}}_j = -\nabla\tilde{P}_j, \tag{33a}$$

$$\partial_t \tilde{P}_j + c_j^2 \nabla\cdot\tilde{\mathbf{U}}_j = 0. \tag{33b}$$

Here $c_j = 1/j\pi$ is the equivalent wavespeed for the baroclinic modes and $c_0 = 1/\sqrt{\alpha}$ is the barotropic wave speed, where $\alpha = N^2H/g$. It is worth recalling that there is a subtlety in the derivation of these modes and wave speeds (see Kelly et al. 2010; Kelly 2016), which is necessary because a naïve treatment with rigid lid boundaries leads to a dynamically inactive barotropic mode with zero phase speed. Instead, a free surface boundary condition is introduced at $z = 1$, an approximation is made in which the barotropic wave speed is assumed large ($\alpha \ll 1$), and then the leading order results in α are retained for each mode. This procedure has the effect of recovering the rigid lid results for the baroclinic modes, while obtaining the correct barotropic wavespeed to leading order in $\alpha^{-1/2}$.

c. Decomposition of the LCPE into kernel cell problems

Once the CCP has been solved, the remaining undetermined quantities in the correlation terms (15a–15b) are the solutions $\{\tilde{\mathbf{u}}_0, \tilde{w}_0, \tilde{b}_0\}$ of the LCPE (14a–14c). The first step in our solution method is to expand the large-scale variables in the vertical basis functions using (27a-27b). It is also necessary to expand the vertical derivatives as

$$\partial_z \mathbf{U}(\mathbf{x},z,t) = \sum_{j=0}^{\infty} \tilde{\mathbf{U}}'_j(\mathbf{x},t)\,\Phi_j(z), \text{ where } \tilde{\mathbf{U}}'_j(\mathbf{x},t) = \frac{1}{c_j^2}\int_0^1 \partial_z \mathbf{U}(\mathbf{x},z',t)\Phi_j(z')\,\mathrm{d}z', \tag{34a}$$

$$\partial_z B(\mathbf{x},z,t) = \sum_{j=0}^{\infty} \tilde{B}'_j(\mathbf{x},t)\phi_j(z), \text{ where } \tilde{B}'_j(\mathbf{x},t) = \int_0^1 \partial_z B(\mathbf{x},z',t)\phi_j(z')\,\mathrm{d}z'. \tag{34b}$$

Inserting these expansions, the LCPE (14a–14c) becomes

$$(\overline{\mathbf{v}}_0\cdot\nabla)\,\tilde{\mathbf{v}}_0 + (\tilde{\mathbf{v}}_0\cdot\nabla)\,\overline{\mathbf{v}}_0 + \nabla\tilde{p}_0 - \tilde{b}_0\mathbf{k} - \nu_0\nabla^2\tilde{\mathbf{v}}_0 = -\sum_{j=0}^{\infty}\left(\tilde{\mathbf{U}}_j\cdot\nabla\right)\overline{\mathbf{v}}_0\phi_j - \sum_{j=0}^{\infty}\overline{w}_0\tilde{\mathbf{U}}'_j\Phi_j, \tag{35a}$$

$$\nabla\cdot\tilde{\mathbf{v}}_0 = 0, \tag{35b}$$

$$(\overline{\mathbf{v}}_0\cdot\nabla)\,\tilde{b}_0 + (\tilde{\mathbf{v}}_0\cdot\nabla)\,\overline{b}_0 + N^2\tilde{w}_0 - \kappa_0\nabla^2\tilde{b}_0 = -\sum_{j=0}^{\infty}\left(\tilde{\mathbf{U}}_j\cdot\nabla\right)\overline{b}_0\phi_j - \sum_{j=0}^{\infty}\overline{w}_0\tilde{B}'_j\phi_j. \tag{35c}$$

Next, the fact that the CCP solutions $\{\overline{\mathbf{v}}_0, \overline{b}_0\}$ are axisymmetric is exploited to write down an ansatz for the solution to the LCPE. That is, it has a simple dependence on the azimuthal variable θ, which is expressed here using the polar coordinate basis vectors $\mathbf{e}_r = (\cos\theta, \sin\theta, 0)^T$ and $\mathbf{e}_\theta = (-\sin\theta, \cos\theta, 0)^T$. The form of the solution to be sought is

$$\begin{aligned}\tilde{\mathbf{v}}_0 = \sum_{j=0}^{\infty} \mathbf{e}_r &\left[\hat{u}^r_{1,j}\left(\tilde{\mathbf{U}}_j\cdot\mathbf{e}_r\right) + \hat{u}^r_{2,j}\left(\tilde{\mathbf{U}}'_j\cdot\mathbf{e}_r\right) + \hat{u}^r_{3,j}\tilde{B}'_j\right] \\ &+ \mathbf{e}_\theta\left[\hat{u}^\theta_{1,j}\left(\tilde{\mathbf{U}}_j\cdot\mathbf{e}_\theta\right) + \hat{u}^\theta_{2,j}\left(\tilde{\mathbf{U}}'_j\cdot\mathbf{e}_\theta\right)\right] \\ &+ \mathbf{k}\left[\hat{w}_{1,j}\left(\tilde{\mathbf{U}}_j\cdot\mathbf{e}_r\right) + \hat{w}_{2,j}\left(\tilde{\mathbf{U}}'_j\cdot\mathbf{e}_r\right) + \hat{w}_{3,j}\tilde{B}'_j\right],\end{aligned} \tag{36a}$$

$$\tilde{p}_0 = \sum_{j=0}^{\infty}\left[\hat{p}_{1,j}\left(\tilde{\mathbf{U}}_j\cdot\mathbf{e}_r\right) + \hat{p}_{2,j}\left(\tilde{\mathbf{U}}'_j\cdot\mathbf{e}_r\right) + \hat{p}_{3,j}\tilde{B}'_j\right], \tag{36b}$$

$$\tilde{b}_0 = \sum_{j=0}^{\infty}\left[\hat{b}_{1,j}\left(\tilde{\mathbf{U}}_j\cdot\mathbf{e}_r\right) + \hat{b}_{2,j}\left(\tilde{\mathbf{U}}'_j\cdot\mathbf{e}_r\right) + \hat{b}_{3,j}\tilde{B}'_j\right], \tag{36c}$$

where the unknowns $\{\hat{u}^r_{k,j}, \hat{u}^\theta_{k,j}, \hat{w}_{k,j}, \hat{p}_{k,j}, \hat{b}_{k,j}\}$, for $k = 1,2,3$ and $j \geq 0$ are each functions of (r,z) only. These unknown functions are determined by three separate 'kernel cell problems' (KCP1,

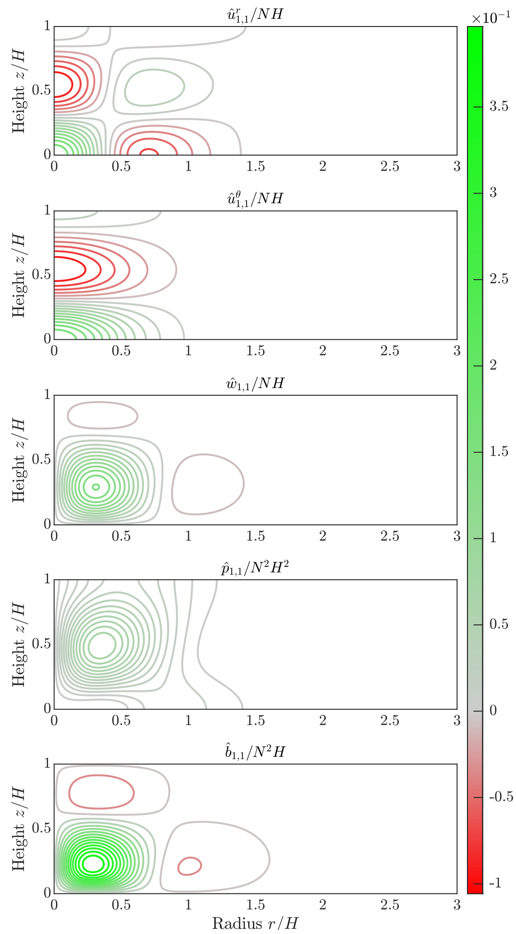

FIG. 3. Contours of the KCP1 solutions $\{\hat{u}^r_{1,1}, \hat{u}^\theta_{1,1}, \hat{w}_{1,1}, \hat{p}_{1,1}, \hat{b}_{1,1}\}$ to (37a) with the boundary conditions (39a–39c). The values $\nu_0 = \kappa_0 = 0.05$ are used.

KCP2, KCP3 hereafter) for each value of k, each which can be used to determine the solution for every value of j. The problems KCP1, KCP2 and KCP3 are found by substituting (36a–36c) into equations (35a–35c) and matching the basis coefficients.

Following this process, KCP1 and KCP2 are found to have the abstract form

$$\mathcal{M}\left(\overline{\psi}_0, \overline{b}_0; r, z\right) \hat{\mathbf{q}}_{1,j}(r,z) = \mathbf{r}_1\left(\overline{\psi}_0, \overline{b}_0; r, z\right) \phi_j(z), \tag{37a}$$

$$\mathcal{M}\left(\overline{\psi}_0, \overline{b}_0; r, z\right) \hat{\mathbf{q}}_{2,j}(r,z) = \mathbf{r}_2\left(\overline{\psi}_0, \overline{b}_0; r, z\right) \Phi_j(z). \tag{37b}$$

Here, $\mathcal{M}$ is a 5×5 linear, elliptic matrix operator (see appendix B for its explicit form) which acts on the vectors $\hat{\mathbf{q}}_{k,j} = (\hat{u}^r_{k,j}, \hat{u}^\theta_{k,j}, \hat{w}_{k,j}, \hat{p}_{k,j}, \hat{b}_{k,j})^T$ for $k = 1, 2$. A key point regarding the efficient numerical solution of the problem is that the discretized form of $\mathcal{M}$ need only be calculated once in order to solve KCP1 and KCP2 for every value of j. The vectors $\mathbf{r}_1$ and $\mathbf{r}_2$ are given by

$$\mathbf{r}_1 = -\begin{pmatrix} \partial_r\left(\frac{1}{r}\partial_z\overline{\psi}_0\right) \\ \frac{1}{r^2}\partial_z\overline{\psi}_0 \\ \partial_r\left(\frac{1}{r}\partial_r\overline{\psi}_0\right) \\ 0 \\ \partial_r\overline{b}_0 \end{pmatrix}, \qquad \mathbf{r}_2 = \frac{1}{r}\partial_r\overline{\psi}_0\begin{pmatrix} 1 \\ 1 \\ 0 \\ 0 \\ 0 \end{pmatrix}. \tag{38a,b}$$

The boundary conditions for KCP1 ($k = 1$) and KCP2 ($k = 2$) are

$$\partial_z\hat{u}^r_{k,j} = \partial_z\hat{u}^\theta_{k,j} = \hat{w}_{k,j} = \hat{b}_{k,j} = 0, \quad \text{at} \quad z = 0, 1, \tag{39a}$$

$$\partial_r\hat{u}^r_{k,j} = \partial_r\hat{u}^\theta_{k,j} = \hat{w}_{k,j} = \hat{p}_{k,j} = \hat{b}_{k,j} = 0, \quad \text{at} \quad r = 0, \tag{39b}$$

$$\hat{u}^r_{k,j} = \partial_r\hat{u}^\theta_{k,j} = \partial_r\hat{w}_{k,j} = \hat{b}_{k,j} = 0, \quad \text{at} \quad r = r_{\text{out}}. \tag{39c}$$

KCP3 is somewhat different to KCP1 and KCP2. Notably, there is no azimuthal component of velocity and so we are able to rewrite the system in streamfunction-vorticity form using the definitions

$$\hat{u}^r_{3,j} = -\frac{1}{r}\partial_z\hat{\psi}_{3,j}, \qquad \hat{w}_{3,j} = \frac{1}{r}\partial_r\hat{\psi}_{3,j}, \tag{40}$$

and

$$\hat{\zeta}_{3,j} = \partial_r\hat{w}_{3,j} - \partial_z\hat{u}^r_{3,j}. \tag{41}$$

In this formulation, KCP3 may be written in terms of the variables $\{\hat{\psi}_{3,j}, \hat{\zeta}_{3,j}, \hat{b}_{3,j}\}$ as

$$\mathcal{N}\left(\overline{\psi}_0, \overline{\zeta}_0, \overline{b}_0; r, z\right)\hat{\mathbf{q}}_{3,j}(r,z) = \mathbf{r}_3\left(\overline{\psi}_0; r, z\right)\phi_j(z). \tag{42}$$

Here, $\mathcal{N}$ is a 3×3 linear, elliptic operator (see appendix B) which acts upon the vector $\hat{\mathbf{q}}_{3,j} = (\hat{\psi}_{3,j}, \hat{\zeta}_{3,j}, \hat{b}_{3,j})^T$, and the vector $\mathbf{r}_3$ is given by

$$\mathbf{r}_3 = -\frac{1}{r}\partial_r\overline{\psi}_0 \begin{pmatrix} 0 \\ 0 \\ 1 \end{pmatrix}. \tag{43}$$

Again, the discretized form of $\mathcal{N}$ need only be calculated once in order to solve KCP3 for every value of j. The boundary conditions are analogous to (23a–23c) used to solve the CCP, and are given by

$$\hat{\psi}_{3,j} = \hat{\zeta}_{3,j} = \hat{b}_{3,j} = 0, \quad \text{on} \quad z = 0, 1, \tag{44a}$$

$$\hat{\psi}_{3,j} = \hat{\zeta}_{3,j} = \partial_r\hat{b}_{3,j} = 0, \quad \text{on} \quad r = 0, \tag{44b}$$

$$\hat{\psi}_{3,j} = \hat{\zeta}_{3,j} = \hat{b}_{3,j} = 0, \quad \text{on} \quad r = r_{\text{out}}. \tag{44c}$$

d. Numerical solutions of the kernel cell problems KCP1, KCP2 and KCP3

Having fully defined the three kernel cell problems KCP1, KCP2 and KCP3 we are now in a position to describe their numerical solution for an example cloud circulation $\{\overline{\mathbf{v}}_0, \overline{b}_0\}$. The cloud circulation we choose is naturally the solution to the CCP described above and illustrated in Figs. 1 and 2. The numerical solutions are found using a Chebyshev collocation method with the same numerical parameters as for the CCP, which are given in appendix A. For an introductory discussion of the Chebychev collocation method, the reader is directed to Trefethen (2000); Boyd (2001).

We first consider the two cell problems KCP1 and KCP2. As an example of the numerical solutions found, Figs. 3 and 4 show the solutions associated with first baroclinic wave mode ($j = 1$) $\{\hat{u}^r_{1,1}, \hat{u}^\theta_{1,1}, \hat{w}_{1,1}, \hat{p}_{1,1}, \hat{b}_{1,1}\}$ to KCP1 and $\{\hat{u}^r_{2,j}, \hat{u}^\theta_{2,j}, \hat{w}_{2,j}, \hat{p}_{2,j}, \hat{b}_{2,j}\}$ to KCP2 respectively. The solutions are centered on the cloud core and decay significantly by the outer domain boundary at $r = r_{\text{out}}$. Qualitatively similar results, albeit with different vertical structures, are found for other values of j up to the vertical truncation to be discussed below.

Similarly, for KCP3, Fig. 5 shows the KCP3 solutions $\{\hat{\psi}_{3,1}, \hat{\zeta}_{3,1}, \hat{b}_{3,1}\}$ associated with the first baroclinic wave mode ($j = 1$). The variables $\{\hat{u}^r_{3,j}, \hat{w}_{3,j}, \hat{p}_{3,j}, \hat{b}_{3,j}\}$ in (36a–36c) can be calculated

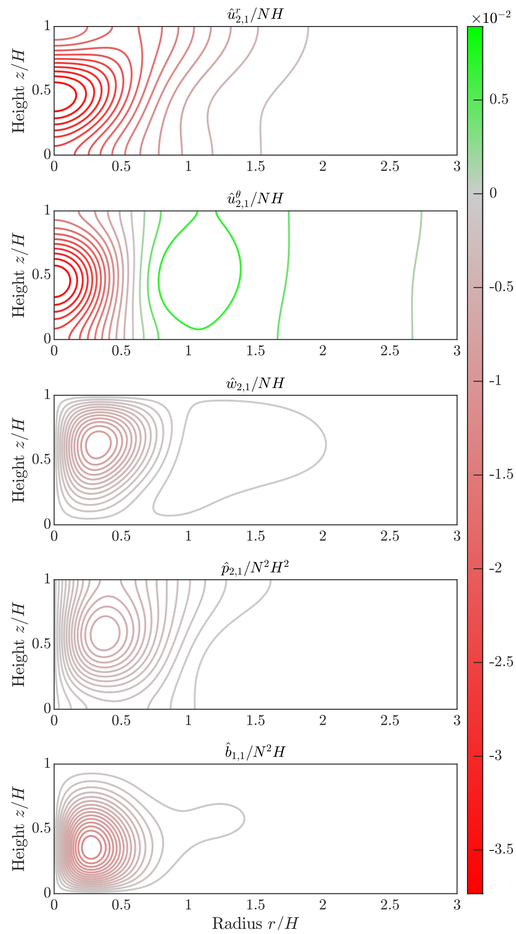

FIG. 4. Contours of the KCP2 solutions $\{\hat{u}^r_{2,1}, \hat{u}^\theta_{2,1}, \hat{w}_{2,1}, \hat{p}_{2,1}, \hat{b}_{2,1}\}$ to (37b) with the boundary conditions (39a–39c). The values $\nu_0 = \kappa_0 = 0.05$ are used.

from $\{\hat{\psi}_{3,j}, \hat{\zeta}_{3,j}, \hat{b}_{3,j}\}$ by Chebyshev differentiation, however it is sufficient to leave them in their current form to calculate the correlation terms in (12a–12d).

e. Calculation of the transilient kernels K_1, K_2 and L

Once the cloud circulation variables $\{\overline{\mathbf{v}}_0, \overline{b}_0\}$ are known from solving the CCP, and the perturbation variables $\{\tilde{\mathbf{u}}_0, \tilde{w}_0, \tilde{b}_0\}$ are known from solving the LCPE via the kernel cell problems KCP1-3, it is then possible to find the vertical flux terms in (15a-15b) and thus calculate the transilient kernels $K_1(z,z')$, $K_2(z,z')$ and $L(z,z')$ which define the operators $\mathcal{K}_1$, $\mathcal{K}_2$ and $\mathcal{L}$ appearing in the homogenized equations (17a-17d).

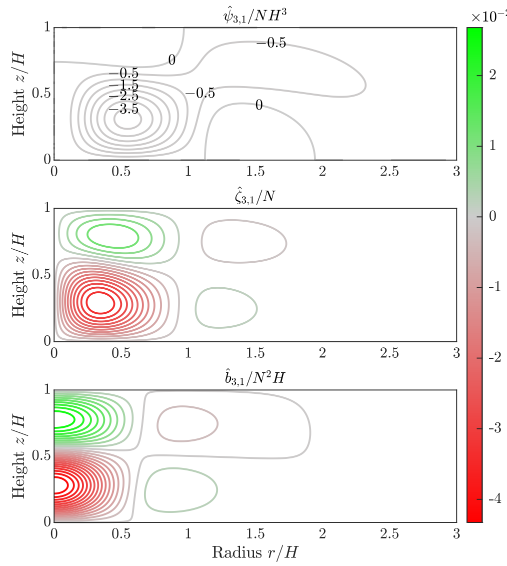

FIG. 5. Contours of the solutions $\{\hat{\psi}_{3,1}, \hat{\zeta}_{3,1}, \hat{b}_{3,1}\}$ to (42) with the boundary conditions (44a–44c). Due to the small magnitude of $\hat{\psi}_{3,1}$, contour values are included in the first panel for clarity, where the numerical value along each contour is understood to be 10^{-4} times the displayed number. The values $\nu_0 = \kappa_0 = 0.05$ are used.

The first step is to insert the ansatz (36a-36c) for $\{\tilde{\mathbf{u}}_0, \tilde{w}_0, \tilde{b}_0\}$ into the formula for the vertical flux terms, and then perform the averaging operation defined by (9). The result is

$$\langle \overline{w}_0 \tilde{\mathbf{u}}_0 + \tilde{w}_0 \overline{\mathbf{u}}_0 \rangle_0 = \sum_{j=0}^{\infty} K_{1,j}(z) \tilde{\mathbf{U}}_j(\mathbf{x}, t) + K_{2,j}(z) \tilde{\mathbf{U}}'_j(\mathbf{x}, t), \tag{45a}$$

$$\langle \overline{w}_0 \tilde{b}_0 + \tilde{w}_0 \overline{b}_0 \rangle_0 = \sum_{j=0}^{\infty} L_j(z) \tilde{B}'_j(\mathbf{x}, t), \tag{45b}$$

where

$$K_{k,j}(z) = \pi \int_0^{\infty} \left(\partial_r \overline{\psi}_0 \left(\hat{u}^r_{k,j} + \hat{u}^\theta_{k,j} \right) - \partial_z \overline{\psi}_0 \hat{w}_{k,j} \right) \, \mathrm{d}r, \quad \text{for} \quad k = 1, 2, \tag{46a}$$

$$L_j(z) = 2\pi \int_0^{\infty} \left(\partial_r \overline{\psi}_0 \hat{b}_{3,j} + \overline{b}_0 \partial_r \hat{\psi}_{3,j} \right) \, \mathrm{d}r. \tag{46b}$$

Note that the factors of π appearing in the above formulas for $K_{k,j}$ and L_j arise because the simple dependence on the azimuthal coordinate in (36a-36c) allows the θ-integral in (9) to be evaluated, leaving only an integral in r. Inserting the expressions (27a-27b) for the coefficients $\tilde{\mathbf{U}}_j$ etc. into

(45a-45b), and comparing the result with (15a-15b), leads to the following expressions for the transilient kernels

$$K_1(z,z') = \sum_{j=0}^{\infty} K_{1,j}(z)\phi_j(z'), \tag{47a}$$

$$K_2(z,z') = -\sum_{j=0}^{\infty} \frac{1}{c_j^2} K_{2,j}(z)\Phi_j(z'), \tag{47b}$$

$$L(z,z') = -\sum_{j=0}^{\infty} L_j(z)\phi_j(z'). \tag{47c}$$

Equations (47a-47c) express the transilient kernels directly in terms of the CCP solution $\{\overline{\mathbf{v}}_0, \overline{b}_0\}$ and the kernel cell problem solutions of KCP1-3, and are therefore ideal for the numerical evaluation of $K_1(z,z')$, $K_2(z,z')$ and $L(z,z')$.

The numerical evaluation is of course performed using the same Chebyshev numerical grid as used for the CCP and LCPE solutions. One associated advantage is that use of Chebyshev spectral methods allows the radial integrals in (46a-46b) to be evaluated to spectral accuracy using Clenshaw-Curtis quadrature (see e.g. Trefethen 2000, Ch.12). The accuracy of the numerical evaluation of the transilient kernels using the formulas above depends on a number of numerical parameters, the most important of which are

1. The number N_z of Chebyshev points in the numerical grid for the CCP and LCPE problems in the vertical direction, spanning the domain $0 \le z \le 1$.

2. The number N_r of Chebyshev points in the numerical grid for the CCP and LCPE problems in the radial direction, spanning the domain $0 \le r \le r_{\text{out}}$.

3. The location of the artificial outer boundary at $r = r_{\text{out}}$.

4. The truncation number N_s of vertical baroclinic modes retained in the sums (47a-47c).

Numerical convergence tests with respect to each of these parameters are described in appendix D.

Numerical solutions for the transilient kernels at $N_z = 81$, $N_r = 31$, $r_{\text{out}} = 5$ and $N_s = 20$ are shown in appendix D to be well-converged. Fig. 6 shows the structure of $K_1(z,z')$, $K_2(z,z')$ and $L(z,z')$ at this resolution. It is notable that $K_1(z,z')$ has a mainly dipolar structure while $K_2(z,z')$ and

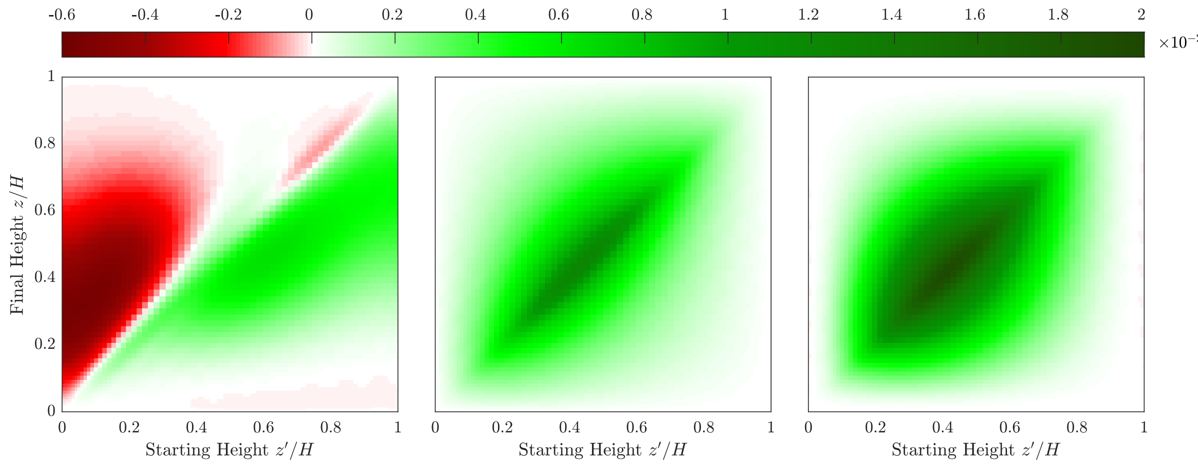

FIG. 6. The transilient kernels $K_1(z,z')$, $K_2(z,z')$ and $L(z,z')$ (left to right). Both z and z' are discretized using a Chebyshev grid with $N_z = 81$ points, and the infinite sum is truncated at $N_s = 20$.

$L(z,z')$ have a monopolar structure. The implications for the behaviour of the operators $\mathcal{K}_1$, $\mathcal{K}_2$ and $\mathcal{L}$ appearing in the homogenized equations (17a-17d) will be discussed in the next section.

4. Behaviour of the homogenized equations (17a–17d)

In this section the properties of the homogenized equations (17a–17d) will be examined, with the main emphasis on the question of how the presence of a cloud field affects the propagation of linear Rossby waves and inertia-gravity waves. First, however, we discuss the physical nature of the non-local operators $\mathcal{K}_1$, $\mathcal{K}_2$ and $\mathcal{L}$ which appear in (17a–17d).

a. Properties of the non-local operators $\mathcal{K}_1$, $\mathcal{K}_2$, $\mathcal{L}$

To gain some intuition about the nature of the nonlinear operators $\mathcal{K}_1$, $\mathcal{K}_2$ and $\mathcal{L}$, it is helpful to briefly review those instances where similar operators have been used to model the effects of turbulent eddies in the atmosphere in related studies (see e.g. Romps and Kuang 2011; Stull 1984; Bhamidipati et al. 2020). In particular, Romps and Kuang (2011) give a helpful discussion of a scenario in which a tracer with mixing ratio $c(z,t)$ undergoes vertical redistribution according to

$$\partial_t c + \mathcal{T} c = 0, \quad \text{where} \quad \mathcal{T} c = \int_0^1 T(z,z')c(z',t)\,\mathrm{d}z', \tag{48}$$

i.e. $\mathcal{T}$ is a non-local transport operator with transilient kernel $T(z,z')$.

When $c(z,t)$ represents a tracer mixing ratio, the operator $\mathcal{T}$ must then obey two important conservation properties. Firstly, assuming c is conserved, it follows that

$$(\text{“\textit{no sink}”}) \quad \int_0^1 \mathcal{T}c \, \mathrm{d}z = 0, \quad \text{or} \int_0^1 T(z,z') \, \mathrm{d}z = 0, \tag{49}$$

which ensures that there is no overall source or sink of tracer. Further, it must also hold that

$$(\text{“\textit{no un-mixing}”}) \quad \mathcal{T}c = 0, \text{ when } c = \text{const}, \quad \text{or} \int_0^1 T(z,z') \, \mathrm{d}z' = 0, \tag{50}$$

since if c is initially constant in z, the tracer profile should remain constant for all time under parcel rearrangement. This property reflects the fact that the eddies may not act to ‘un-mix’ the fluid, as has also been discussed in the context of (potential) vorticity mixing (Shnirelman 1993; Wood and Mcintyre 2009; Shnirelman 2013).

While the above properties of $\mathcal{T}$ are a helpful reference point, particularly for understanding the action of $\mathcal{K}_1$ which from Fig. 6 appears close to satisfying the same integral properties, the non-local terms in (17a–17d) are clearly more complicated. Nevertheless, it is clear that the additional z-derivatives which appear in (17a–17d) ensure that, as expected, there is no generation of total buoyancy or horizontal momentum due to the presence of the clouds, i.e. they obey the ‘no sink’ property above. Another useful reference point is to consider a localized limit, in which the patterns seen in Fig. 6 are projected onto the diagonal $z = z'$, i.e.

$$K_1(z,z') \approx -\kappa_U(z)\delta'(z-z') + W_U(z)\delta(z-z') \qquad \text{(Dipole+Monopole)}, \tag{51a}$$

$$K_2(z,z') \approx \kappa_{U'}(z)\delta(z-z') \qquad \text{(Monopole)}, \tag{51b}$$

$$L(z,z') \approx \kappa_{B'}(z)\delta(z-z') \qquad \text{(Monopole)}, \tag{51c}$$

where $\delta(z)$ is the Dirac delta distribution. Under this approximation the terms involving the non-local operators simplify as follows

$$\partial_z\left(\mathcal{K}_1 \boldsymbol{U}\right) \approx -\partial_z\left(\kappa_U \partial_z \mathbf{U}\right) + \partial_z(W_U \mathbf{U}), \tag{52a}$$

$$\partial_z\left(\mathcal{K}_1 \partial_z \boldsymbol{U}\right) \approx \partial_z\left(\kappa_{U'} \partial_z \mathbf{U}\right), \tag{52b}$$

$$\partial_z\left(\mathcal{L} \partial_z B\right) \approx \partial_z\left(\kappa_{B'} \partial_z B\right). \tag{52c}$$

Hence the dipolar component of $\mathcal{K}_1$ and monopolar components of $\mathcal{K}_2$ and $\mathcal{L}$ each become simple vertical diffusion terms for horizontal momentum and buoyancy. It seems reasonable to conclude that the primary action of each operator is to act as a non-local vertical diffusion, with $\mathcal{K}_1$ also contributing a non-local vertical advection due to its monopolar component. Note that a similar non-local operator in the buoyancy equation (17d) has been obtained by Bhamidipati et al. (2020), with a similar interpretation given.

A further consideration concerns whether the $\mathcal{K}_1$ operator satisfies the *no un-mixing* property. Evaluating the relevant integral

$$\int_0^1 \partial_z K_1(z, z')\, \mathrm{d}z' = \partial_z K_{1,0}(z) \phi_0(1) \neq 0, \tag{53}$$

shows that it is not satisfied, implying that a horizontal momentum profile which is initially constant in z may develop vertical variations in the presence of a cloud field. Importantly, horizontal momentum is not transported as a tracer in the homogenized equations (17a–17d), and so no physical laws are violated by this fact. It is perhaps more insightful for the purposes of this subsection to recognize that after integrating by parts, the term involving $\mathcal{K}_1$ may be rewritten as

$$\partial_z \int_0^1 K_1(z, z') \mathbf{U}(z')\, \mathrm{d}z' = \partial_z J(z, 1) \mathbf{U}(1) - \partial_z \left(\int_0^1 J(z, z') \partial_z \mathbf{U}(z')\, \mathrm{d}z' \right), \tag{54}$$

where $\partial_{z'} J(z, z') = K_1(z, z')$. Thus, this operator may be viewed as a term which partially contributes to the non-local vertical diffusion of horizontal momentum (much like the term involving $\mathcal{K}_2$), but simultaneously adds a horizontal, height dependent forcing, proportional to the velocity field at the free surface. Consequently, a velocity field which is vertically uniform at time $t = 0$ is instantaneously subject only to the surface forcing, so that vertical variations develop for $t > 0$.

b. Numerical solution of the homogenized equations (17a–17d)

In order to answer the key scientific question of how the dispersion relations of Rossby and inertia-gravity waves change when n is non-zero, plane-wave solutions of (17a–17d) can be sought in a β-channel with sidewalls at $y = \pm 1$. Physically, this corresponds to a channel half-width of one Rossby radius. First, the variables W and B are eliminated from (17a–17d) in favour of $\mathbf{U}$ and P, and then plane-wave solutions are sought using the ansatz

$$[\mathbf{U}, P]\,(\mathbf{x}, z, t) = \sum_{j=0}^{\infty} \left[\hat{\mathbf{U}}_j(y), \hat{P}_j(y)\right] \phi_j(z) \exp\left(\mathrm{i}kx - \mathrm{i}\omega t\right). \tag{55}$$

Details of the working are given in appendix C. The result is an eigenvalue problem, in which the wave frequency ω takes the role of the eigenvalue, which is constituted by the following infinite set of coupled ordinary differential equations

$$-\mathrm{i}n \sum_{m=0}^{\infty} \left(\tilde{C}_{j,m} - \tilde{D}_{j,m}\right) \hat{U}_m + \mathrm{i} f \hat{V}_j + k \hat{P}_j = \omega \hat{U}_j, \tag{56a}$$

$$-\mathrm{i} f \hat{U}_j - \mathrm{i}n \sum_{m=0}^{\infty} \left(\tilde{C}_{j,m} - \tilde{D}_{j,m}\right) \hat{V}_m + \frac{\mathrm{d}\hat{P}_j}{\mathrm{d}y} = \omega \hat{V}_j, \tag{56b}$$

$$k c_j^2 \hat{U}_j - \mathrm{i} c_j^2 \frac{\mathrm{d}\hat{V}_j}{\mathrm{d}y} + \mathrm{i}n \sum_{m=0}^{\infty} \left(\frac{c_j}{c_m}\right)^2 \tilde{E}_{j,m} \hat{P}_m = \omega \hat{P}_j, \tag{56c}$$

with boundary conditions $\hat{V}_j(\pm 1) = 0$ for $j = 0, 1, 2, \ldots$. The coefficients $\tilde{C}_{j,m}$, $\tilde{D}_{j,m}$ and $\tilde{E}_{j,m}$ are given in appendix C.

In order to solve (56a-56c) numerically, parameter values must first be chosen. Recalling that here $f = 1 + \bar{\beta} y$, the non-dimensional β-parameter is taken to be $\bar{\beta} = 0.1$, since this corresponds to a dimensional value of $\beta \sim 10^{-11}\mathrm{m}^{-1}\mathrm{s}^{-1}$, which is appropriate for the mid-latitude atmosphere. Next, a representative value of the cloud density $\overline{n}$ must be chosen. A value for the scaled number density $n = 5$ is used here, which in the parameter set-up for the troposphere ($\varepsilon \approx 0.01$) corresponds to a number density of $\overline{n} = 0.05$. This constitutes a relatively sparse array of clouds - specifically, one cloud per 20 non-dimensional units of horizontal area, so that the average spacing between clouds is $D_{\mathrm{avg}} \sim \sqrt{20} \approx 4.47$. In dimensional terms, this corresponds to the distance between heat sources being approximately 4.5 times the height of the tropopause ($\approx 4.5 \times 10$km). In terms of the β–channel set-up used here, this means that on average, approximately 44 clouds may span its breadth. Importantly, these average spacing distances are sufficiently large to justify the approximation in section 2 that individual clouds interact only linearly, since it is clear from Fig. 1 and Figs. 3–5 that the dynamics introduced by clouds have decayed substantially when $r \sim D_{\mathrm{avg}}/2$.

The eigenvalue problem defined by (56a-56c) is discretized by truncating the number of vertical baroclinic modes at $N_s = 9$ (convergence with respect to N_s is shown to be rapid in appendix D) and introducing a discrete Chebyshev grid in the y-direction using $N_y = 26$ Chebyshev points. The result is a standard linear algebra eigenvalue problem with a block matrix structure of dimension $3(N_s+1)N_y \times 3(N_s+1)N_y = 760 \times 760$. This eigenvalue problem is then solved repeatedly, using a standard linear algebra package, for many values of the wavenumber k in order to generate the dispersion relations to be discussed below.

c. Results: Rossby and inertia-gravity wave dispersion relations in the presence of clouds

Fig. 7 shows the real part of the frequencies from the calculated dispersion relations for some of the most important wave modes calculated in the β-channel for the parameter settings detailed above. The solid curves in each panel show the dispersion relation in the absence of clouds ($n = 0$) and the dotted curves show the results when clouds are present ($n = 5$). In each panel, the red, green and blue curves correspond to the leading three cross-channel modes, i.e. they are distinguished by their meridional structure. The left panels show the barotropic mode, the middle panels the first baroclinic mode, and the right panels the second baroclinic mode. The inertia-gravity wave mode dispersion relations are plotted in the upper panels and the Rossby wave dispersion relations in the lower panels (note the different frequency ranges). It should be noted that Kelvin wave solutions are also present in the system (56a–56c), however these are omitted since the existence of the Kelvin wave depends upon the presence of the sidewalls. In the mid-latitude troposphere, there are no equivalent boundaries or waveguides, hence they are not physical.

Fig. 7 allows the changes to the dispersion relations due to the clouds to be assessed on a mode-by-mode basis. First, we see that all of the barotropic wave modes are almost entirely unaffected by the cloud field. Mathematically, this arises from the fact that integrating the homogenized equations (17a–17d) over the vertical domain causes the terms due to convection to vanish. Small residual effects exist due to the barotropic waves not being exactly homogeneous in the vertical,

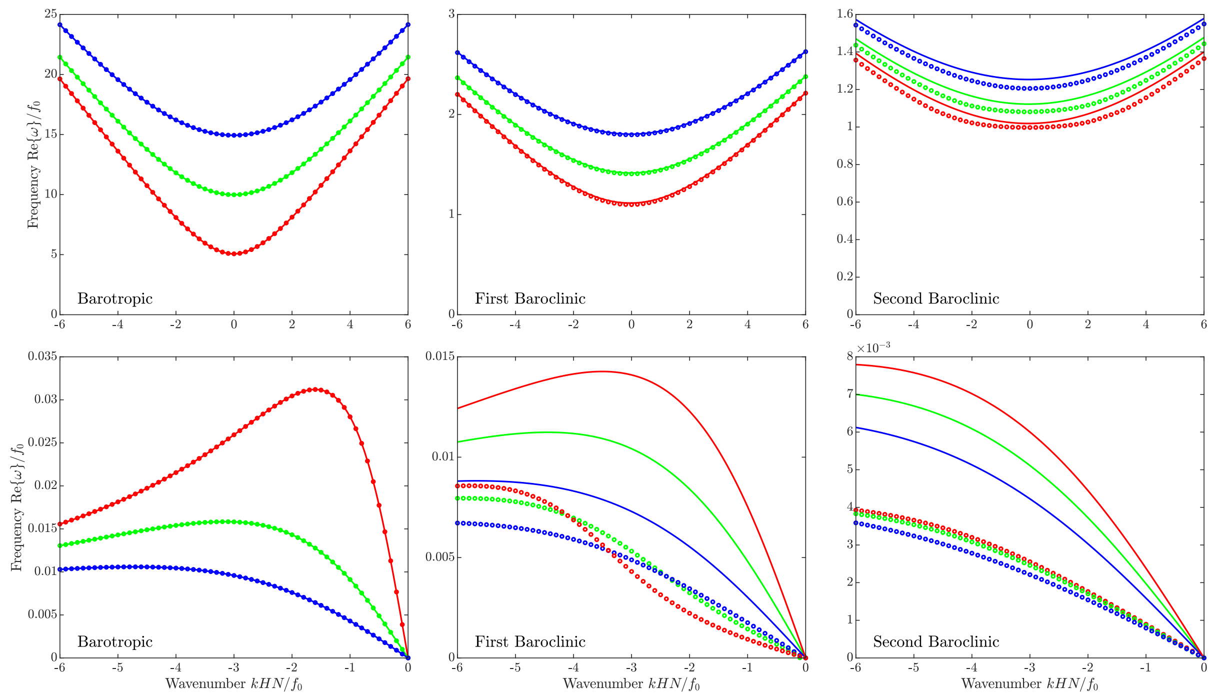

FIG. 7. Dispersion relations for the barotropic, first baroclinic and second baroclinic wave modes (left, centre and right columns respectively). In the top row the first three cross-channel inertia-gravity modes are shown (red, green, blue), and in the bottom row the first three Rossby wave modes are shown. The line plots indicate wave propagation through a cloud-free atmosphere calculated from (33a) and (33b) and the circles indicate the corresponding waves when clouds are present, calculated from (C1a) and (C1b). The numerical parameters are $\bar{\beta} = 0.1$ and $n = 5$, and the equivalent wave speeds for each vertical wave mode are $c_0 = 1/\sqrt{\alpha}$, $c_1 = 1/\pi$ and $c_2 = 1/2\pi$.

are present in the numerical calculations due to the error introduced by the rigid lid / free surface approximations discussed above. In summary, the barotropic modes are unaffected by convection to leading order in the rigid lid approximation.

Considering next the first baroclinic mode (middle panels), it is evident that the inertia-gravity waves are only slightly affected by the clouds, with their frequencies deviating only marginally from their counterparts in a cloud-free atmosphere. In contrast, the Rossby waves are seen to be significantly slowed by convection, with some frequencies being reduced by over half at small wave numbers compared to their cloud-free analogues. Furthermore, the lower order cross-channel modes are more significantly slowed than the higher order modes, especially at smaller zonal wave numbers, indicating that for the first baroclinic mode the smallness of the total wave number is

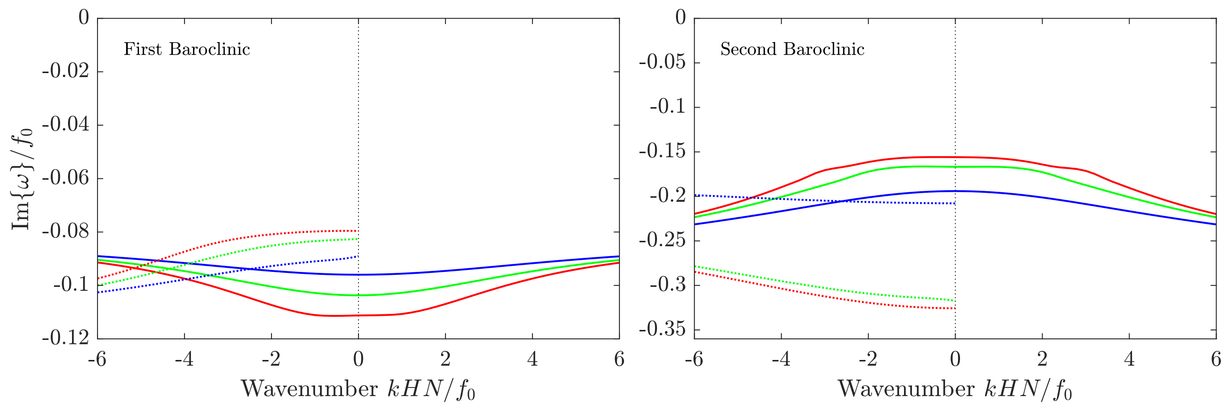

Fig. 8. Plots of $\mathrm{Im}\{\omega\}$ for the first and second baroclinic modes (left and right panels respectively). The first three cross channel modes (red, green, blue) are shown for the inertia-gravity waves (solid lines) and Rossby waves (dotted lines).

highly significant in determining the extent to which the clouds impact wave propagation. An explanation for the large impact on the first baroclinic mode is that the heating profile (25) has a vertical structure which vanishes at $z = 0, 1$ and has maximum value in the middle of the domain. Thus it is qualitatively similar in form to the vertical structure of the first baroclinic vertical velocity and buoyancy wave modes. Consequently, the forcing due to the cloud field projects most strongly onto this mode and it therefore experiences the largest impact. Further analysis of the relationship between the heating profile, the structure of the CCP solution, and the impact on the propagation of different wave modes will be pursued in a future study.

Finally, in the case of the second baroclinic mode, all wave types are noticeably slowed by the presence of clouds. Once again, we see that the waves most affected are the Rossby waves. However, in contrast to the first baroclinic mode, it appears that the wavenumber is no longer such a significant factor in determining the effect of the clouds on wave dispersion. For example, Rossby wave frequencies are approximately halved almost independently of the zonal or meridional wavenumber. At present we don't have an explanation for why the sensitivity to wavenumber is significant for the first baroclinic mode but not the second.

The presence of the cloud field also has a significant damping effect on all the first and second baroclinic waves in the β-channel. Fig. 8 shows the imaginary part of the frequencies for these modes. Negative values $\mathrm{Im}\{\omega\}$, which are found for all wave modes, correspond to exponential decay rates. The damping effect is approximately doubled for the second baroclinic mode compared to the first, and it is found in general that the damping affects higher order baroclinic modes more strongly, consistent with the cloud terms in (17a–17d) acting as a vertical diffusion. There is also found to be only minor differences in the magnitude of the damping between the inertia-gravity modes and Rossby wave modes for each baroclinic mode.

In summary, barotropic modes are unaffected by the stationary cloud field, whilst baroclinic modes feel the effects strongly, with the most strongly affected waves being Rossby wave modes of low frequency. The fact that the first baroclinic Rossby wave modes are affected most strongly is likely because the forcing from the heat source and the resulting circulation projects most strongly onto this vertical mode.

5. Conclusions

The main contribution of this work is to demonstrate that the effect of small-scale nonlinear convective circulations can be represented in large-scale dynamical equations systematically using the method of homogenization. It should be clear that there is potential for developing this method to improve the parameterization of atmospheric convection, by accounting for the dynamics of individual convective clouds through a multiple-scales asymptotic procedure, rather than relying upon heuristics to model their interaction with the large-scale flow. It is encouraging that the non-local operators which emerge in our study are based on transilient kernels, and act as non-local vertical diffusion and forcing terms in the large-scale equations. These features suggest that the results from the homogenization methodology can be translated into systematic closures for convective parameterizations which structurally resemble existing schemes.

Further proof of the potential value of improving the representation of convective parameterizations in large-scale models is provided by Fig. 7, which shows the impact that a plausible cloud field has on the frequencies of the first baroclinic Rossby waves. The implications for forecasts of such a large effect are profound and, even after allowance is made for possible overestimation of the effect due to the simplifications in our model, any improvement in the representation of unresolved circulations is going to have a significant positive impact on models. While here we focussed on the mid-latitude atmosphere, our approach is equally valid in equatorial regions and will be used in future to investigate the many convective features of the tropics, such as the Madden-Julian Oscillation.

Of course, the present study constitutes only a first step, and various assumptions and approximations have been made to simplify the analysis which need to be relaxed if the results are to be used in a more practical setting. The most significant of these are that the clouds are stationary, that the moisture field is not dynamically active, and that the individual cumulus clouds are well-separated. It is the authors' view that there is no obstacle in principle to relaxing the first two assumptions, i.e. the method could be applied to a time-dependent CCP with a dynamic moisture field to obtain a time-dependent relationship between the vertical fluxes and the large-scale flow. The assumption of well-separated clouds, however, is central to the asymptotic approach employed here and (apart from continuing the asymptotic expansion to higher order in ε, which is unlikely to be productive) must be retained. A further aspect is that only the linear large-scale equations have been incorporated into the analysis here. Homogenization can be applied to nonlinear equations (Vanneste 2003; Radko 2022a,b) but typically at the cost of further simplifying assumptions which need to be investigated.

We end by noting that the homogenization approach to parameterization could connect well with another emerging body of work. For example, Igel and Biello (2020) have introduced an approach to modelling convection using the "DoNUT" (the dynamics of non-rotating updraft torii). This model, which calculates solutions which are analogous to the CCP solution shown here in Fig. 1, aims to capture convective cloud circulations more accurately than a single column model. The utility of such a cloud model within convective parameterizations could be tractably tested within the framework outlined in this paper, and will be a topic of future study.

Acknowledgments. The authors gratefully acknowledge support from the NERC and UK Met Office case award NE/P009468/1. EJG acknowledges additional student support from University College London.

APPENDIX A

Numerical solution of the CCP

The nonlinear system (22a–22c) is solved using an iterative procedure based on a quasi-linearization method (see e.g. Motsa et al. 2014; Muzara et al. 2018). We begin by assuming there exist sequences of approximants for $\overline{\psi}_0, \overline{\zeta}_0, \overline{b}_0$, with the mth iterates denoted by $\overline{\psi}_0^{(m)}, \overline{\zeta}_0^{(m)}, \overline{b}_0^{(m)}$, such that

$$\left(\overline{\psi}_0^{(m)}, \overline{\zeta}_0^{(m)}, \overline{b}_0^{(m)}\right) \rightarrow \left(\overline{\psi}_0, \overline{\zeta}_0, \overline{b}_0\right) \quad \text{as} \quad m \rightarrow \infty. \tag{A1}$$

The method is based upon approximating the nonlinear terms at the $(m+1)$th iteration in the CCP as, for example

$$\begin{aligned} \mathcal{J}\left(\overline{\psi}_0^{(m+1)}, \overline{b}_0^{(m+1)}\right) \approx \mathcal{J}\left(\overline{\psi}_0^{(m+1)}, \overline{b}_0^{(m)}\right) + \\ \mathcal{J}\left(\overline{\psi}_0^{(m)}, \overline{b}_0^{(m+1)}\right) - \mathcal{J}\left(\overline{\psi}_0^{(m)}, \overline{b}_0^{(m)}\right). \end{aligned} \tag{A2}$$

Therefore, the $(m+1)$th iteration is found in terms of the mth iterate (which is assumed known) from the solution to the linear system

$$\begin{aligned} \mathcal{J}\left(\overline{\psi}_0^{(m+1)}, \overline{\zeta}_0^{(m)}/r\right) + \mathcal{J}\left(\overline{\psi}_0^{(m)}, \overline{\zeta}_0^{(m+1)}/r\right) - \partial_r \overline{b}_0^{(m+1)} \\ = \nu_0 \left(\nabla^2 \overline{\zeta}_0^{(m+1)} - \frac{\overline{\zeta}_0^{(m+1)}}{r^2}\right) + \mathcal{J}\left(\overline{\psi}_0^{(m)}, \overline{\zeta}_0^{(m)}/r\right), \end{aligned} \tag{A3}$$

$$\overline{\zeta}_0^{(m+1)} = \frac{1}{r}\left(\partial_{rr}^2 \overline{\psi}_0^{(m+1)} - \frac{1}{r}\partial_r \overline{\psi}_0^{(m+1)} + \partial_{zz}^2 \overline{\psi}_0^{(m+1)}\right), \tag{A4}$$

$$\begin{aligned} \frac{1}{r}\mathcal{J}\left(\overline{\psi}_0^{(m+1)}, \overline{b}_0^{(m)}\right) + \frac{1}{r}\mathcal{J}\left(\overline{\psi}_0^{(m)}, \overline{b}_0^{(m+1)}\right) + \frac{1}{r}\partial_r \psi_0^{(m+1)} \\ = Q_0 + \kappa_0 \nabla^2 \overline{b}_0^{(m+1)} + \frac{1}{r}\mathcal{J}\left(\overline{\psi}_0^{(m)}, \overline{b}_0^{(m)}\right). \end{aligned} \tag{A5}$$

The 0th iterate is taken to be the solution to the original linear system (i.e. the solution to (22a–22c) in the absence of the nonlinear terms).

With the problem specified on a finite domain $(r, z) \in [0, r_{\text{out}}] \times [0, 1]$, equations (A3–A5) are discretized using a Chebyshev collocation method, with $N_r = 31$ points in the radial, and $N_z = 81$ points in the vertical directions. The boundary conditions (23a–23c) are implemented in this formulation by altering the outer rows and columns in each block of the resulting block matrix (details omitted), and it is found that using $r_{\text{out}} = 5$ is sufficient to approximate the decay conditions.

APPENDIX B

Explicit formulation of the Kernel Cell Problems

For $k = 1, 2$, the 5×5 elliptic operator $\mathcal{M}(\overline{\psi}_0, \overline{b}_0; r, z)$ associated with KCP1 and KCP2 acts upon the vector $\hat{\mathbf{q}}_{k,j}$ to give a 5 dimensional column vector with entries

$$\begin{aligned}\left(\mathcal{M}\hat{\mathbf{q}}_{k,j}\right)_1 = {} & \frac{1}{r}\partial_z\overline{\psi}_0\partial_r\hat{u}^r_{k,j} + \partial_r\left(\frac{1}{r}\partial_r\overline{\psi}_0\right)\hat{u}^r_{k,j} - \frac{1}{r}\partial_r\overline{\psi}_0\partial_z\hat{u}^r_{k,j} + \hat{w}_{k,j}\partial^2_{zz}\overline{\psi}_0 - \partial_r\hat{p}_{k,j} \\ & + \nu_0\left(\frac{1}{r}\partial_r\left(r\partial_r\hat{u}^r_{k,j}\right) - \frac{2}{r^2}\left(\hat{u}^r_{k,j} - \hat{u}^\theta_{k,j}\right) + \partial^2_{zz}\hat{u}^r_{k,j}\right),\end{aligned} \tag{B1}$$

$$\begin{aligned}\left(\mathcal{M}\hat{\mathbf{q}}_{k,j}\right)_2 = {} & \frac{1}{r}\partial_z\overline{\psi}_0\partial_r\hat{u}^\theta_{k,j} + \frac{\hat{u}^\theta_{k,j}}{r^2}\partial_z\overline{\psi}_0 - \frac{1}{r}\partial_r\overline{\psi}_0\partial_z\hat{u}^\theta_{k,j} - \frac{1}{r}\hat{p}_{k,j} \\ & + \nu_0\left(\frac{1}{r}\partial_r\left(r\partial_r\hat{u}^\theta_{k,j}\right) + \frac{2}{r^2}\left(\hat{u}^r_{k,j} - \hat{u}^\theta_{k,j}\right) + \partial^2_{zz}\hat{u}^r_{k,j}\right),\end{aligned} \tag{B2}$$

$$\begin{aligned}\left(\mathcal{M}\hat{\mathbf{q}}_{k,j}\right)_3 = {} & \partial_r\left(\frac{1}{r}\partial_r\overline{\psi}_0\right)\hat{u}^r_{k,j} - \frac{1}{r}\partial_z\overline{\psi}_0\partial_r\hat{w}_{k,j} + \frac{1}{r}\partial_r\overline{\psi}_0\partial_z\hat{w}_{k,j} + \frac{\hat{w}_{k,j}}{r}\partial^2_{rz}\overline{\psi}_0 \\ & + \partial_z\hat{p}_{k,j} - \hat{b}_{k,j} - \nu_0\left(\frac{1}{r}\partial_r\left(r\partial_r\hat{w}_{k,j}\right) - \hat{w}_{k,j} + \partial^2_{zz}\hat{w}_{k,j}\right),\end{aligned} \tag{B3}$$

$$\left(\mathcal{M}\hat{\mathbf{q}}_{k,j}\right)_4 = \frac{1}{r}\partial_r\left(r\hat{u}^r_{k,j}\right) - \frac{\hat{u}^\theta_{k,j}}{r} + \partial_z\hat{w}_{k,j}, \tag{B4}$$

$$\begin{aligned}\left(\mathcal{M}\hat{\mathbf{q}}_{k,j}\right)_5 = {} & \hat{u}^r_{k,j}\partial_r\overline{b}_0 + \hat{w}_{k,j}\left(\partial_z\overline{b}_0 + 1\right) - \frac{1}{r}\partial_z\overline{\psi}_0\partial_r\hat{b}_{k,j} + \frac{1}{r}\partial_r\overline{\psi}_0\partial_z\hat{b}_{k,j} \\ & - \kappa_0\left(\frac{1}{r}\partial_r\left(r\partial_r\hat{b}_{k,j}\right) - \frac{1}{r^2}\hat{b}_{k,j} + \partial^2_{zz}\hat{b}_{k,j}\right).\end{aligned} \tag{B5}$$

The 3×3 elliptic operator $\mathcal{N}(\overline{\psi}_0, \overline{\zeta}_0, \overline{b}_0; r, z)$ associated with KCP3 acts on the vector $\hat{\mathbf{q}}_{3,j}$ to give a 3 dimensional column vector with entries

$$\left(\mathcal{N}\hat{\mathbf{q}}_{3,j}\right)_1 = \mathcal{J}\left(\overline{\psi}_0, \frac{\hat{\zeta}_{3,j}}{r}\right) + \mathcal{J}\left(\hat{\psi}_{3,j}, \frac{\overline{\zeta}_0}{r}\right) - \partial_r \hat{b}_{3,j} - \nu_0\left(\frac{1}{r}\partial_r\left(r\partial_r\hat{\zeta}_{3,j}\right) - \frac{\hat{\zeta}_{3,j}}{r^2} + \partial^2_{zz}\hat{\zeta}_{3,j}\right), \tag{B6}$$

$$\left(\mathcal{N}\hat{\mathbf{q}}_{3,j}\right)_2 = \hat{\zeta}_{3,j} - \frac{1}{r}\left(\partial^2_{rr}\hat{\psi}_{3,j} - \frac{1}{r}\partial_r\hat{\psi}_{3,j} + \partial^2_{zz}\hat{\psi}_{3,j}\right), \tag{B7}$$

$$\left(\mathcal{N}\hat{\mathbf{q}}_{3,j}\right)_3 = \frac{1}{r}\mathcal{J}\left(\overline{\psi}_0, \hat{b}_{3,j}\right) + \frac{1}{r}\mathcal{J}\left(\hat{\psi}_{3,j}, \overline{b}_0\right) + \frac{1}{r}\partial_r\hat{\psi}_{3,j} - \kappa_0\left(\frac{1}{r}\partial_r\left(r\partial_r\hat{b}_{3,j}\right) + \partial^2_{zz}\hat{b}_{3,j}\right). \tag{B8}$$

APPENDIX C

Derivation of equations (56a–56c)

Here some additional mathematical details are presented relating to the derivation of (56a–56c). The first step is to expand the homogenized equations (17a–17d) by inserting the expansions (27a) and (27b). Particular care must be taken when determining the coefficients in the modal decomposition of the integral terms, which requires projecting the transilient kernels onto the basis functions $\phi_j(z)$ and $\Phi_j(z)$. The variables $\tilde{W}_j$ and $\tilde{B}_j$ can then be eliminated, resulting in the system

$$\partial_t\tilde{\mathbf{U}}_j + f\mathbf{k}\times\tilde{\mathbf{U}}_j + n\sum_{m=0}^{\infty}\left(\tilde{C}_{j,m} - \tilde{D}_{j,m}\right)\tilde{\mathbf{U}}_m = -\nabla_{\mathbf{x}}\tilde{P}_j, \tag{C1a}$$

$$\partial_t\tilde{P}_j - n\sum_{m=0}^{\infty}\left(\frac{c_j}{c_m}\right)^2\tilde{E}_{j,m}\tilde{P}_m + c_j^2\nabla_{\mathbf{x}}\cdot\tilde{\mathbf{U}}_j = 0, \tag{C1b}$$

for $j = 0, 1, 2, \ldots$, where the coefficients $\tilde{C}_{j,m}$, $\tilde{D}_{j,m}$ and $\tilde{E}_{j,m}$ are given by

$$\tilde{C}_{j,m} = \int_0^1 \frac{1}{c_j^2}K_{1,m}(z)\Phi_j(z)\,\mathrm{d}z, \tag{C2a}$$

$$\tilde{D}_{j,m} = \int_0^1 \frac{1}{c_j^2 c_m^2}K_{2,m}(z)\Phi_j(z)\,\mathrm{d}z, \tag{C2b}$$

$$\tilde{E}_{j,m} = \int_0^1 \frac{1}{c_j^2}L_m(z)\phi_j(z)\,\mathrm{d}z. \tag{C2c}$$

Next, seeking plane wave solutions of the form

$$\left[\tilde{\mathbf{U}}_j(\mathbf{x},t),\tilde{P}_j(\mathbf{x},t)\right]=\left[\hat{\mathbf{U}}_j(y),\hat{P}_j(y)\right]\exp\left(-\mathrm{i}\omega t+\mathrm{i}kx\right), \tag{C3}$$

leads directly to the coupled, infinite linear system of ODEs (56a–56c) given in the main text.

APPENDIX D

Numerical convergence of the transilient kernels

a. Convergence as a function of the truncation number N_s

The convergence of the transilient kernels as a function of the truncation number N_s is now investigated. Firstly, we define the truncated matrices as, for example

$$K_1^{N_s}(z,z')=\sum_{j=0}^{N_s}K_{1,j}(z)\phi_j(z'), \tag{D1}$$

so that we may then define a step-wise error for the matrix $K_1^{N_s}$ as

$$E_{K_1}^{N_s}=\frac{\|K_1^{N_s}-K_1^{N_s-1}\|_{L^2}}{\|K_1^{N_s}\|_{L^2}}, \tag{D2}$$

where $\|\cdot\|_{L^2}$ is the L^2-norm. Fig. D1 shows a log-log plot of the errors $E_{K_1}^{N_s}$, $E_{K_2}^{N_s}$ and $E_L^{N_s}$ as functions of N_s for fixed $N_z=81$, $N_r=31$ and $r_{\text{out}}=5$, and where $E_{K_2}^{N_s}$ and $E_L^{N_s}$ are defined analogously to (D2). The dashed line in the figure is calculated using a least squares regression method on the average of the three errors for mode numbers $N_s\geq 6$. The gradient of this line is found to be $\mu\approx-2.00$, indicating that the errors decay as $E_{K_1}^{N_s},E_{K_2}^{N_s},E_L^{N_s}\sim 1/N_s^2$. Importantly, the errors decrease at an algebraic rate faster than $1/N_s$, and therefore may not accumulate at each step to cause the total error to diverge as $N_s\rightarrow\infty$.

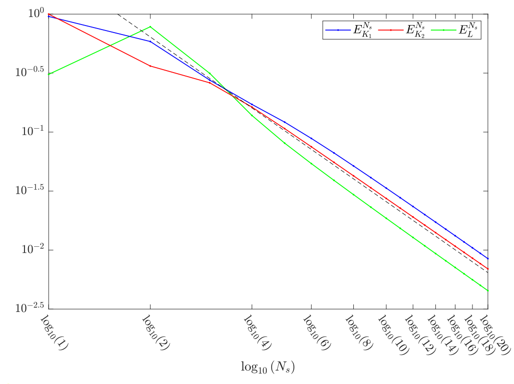

FIG. D1. log-log plot of the step-wise errors in the transilient kernels as a function of N_s. The parameters $N_z = 81$, $N_r = 31$ and $r_{\text{out}} = 5$ are fixed. The dashed line is a linear approximant to the average error for $N_s \geq 6$ calculated using a least squares regression method, the gradient of which is approximately -2.00.

b. Convergence in the radial domain

To test the convergence of the kernels as functions of both N_r and r_{out}, we define two further errors as

$$E_{K_1}^{N_r} = \frac{\|K_1^{N_r} - K_1^{N_r-2}\|_{L^2}}{\|K_1^{N_r}\|_{L^2}}, \tag{D3a}$$

$$E_{K_1}^{r_{\text{out}}} = \frac{\|K_1^{r_{\text{out}}} - K_1^{r_{\text{out}}-1}\|_{L^2}}{\|K_1^{r_{\text{out}}}\|_{L^2}}, \tag{D3b}$$

where $K_1^{N_r}$ and $K_1^{r_{\text{out}}}$ are given by (D1) with $N_s = 20$. In $K_1^{N_r}$, the $K_{1,j}$'s are calculated using N_r radial Chebyshev points with $r_{\text{out}} = 5$ fixed, and in $K_1^{r_{\text{out}}}$, the $K_{1,j}$'s are calculated using $N_r = 31$ Chebyshev points whilst r_{out} may vary. In both cases $N_z = 81$ is fixed.

The top panel of Fig. D2 shows log plots of $E_{K_1}^{N_r}$, $E_{K_2}^{N_r}$ and $E_L^{N_r}$ as functions of N_r. Their decay in the log plot is approximately linear, indicating that their actual decay rate is exponential and that our numerical method has spectral accuracy in the radial direction. The dashed line in this panel is calculated using a least squares regression method based on the average of the three errors, and is found to have a gradient of approximately -0.22, indicating that the errors decay as $E_{K_1}^{N_r}, E_{K_2}^{N_r}, E_L^{N_r} \sim \exp(-0.22 N_r)$.

The bottom panel of Fig. D2 shows log-log plots of $E_{K_1}^{r_{\text{out}}}$, $E_{K_2}^{r_{\text{out}}}$ and $E_L^{r_{\text{out}}}$ as functions of r_{out}. The errors are seen to decrease rapidly at first (approximately linearly on the log-log plot, corresponding

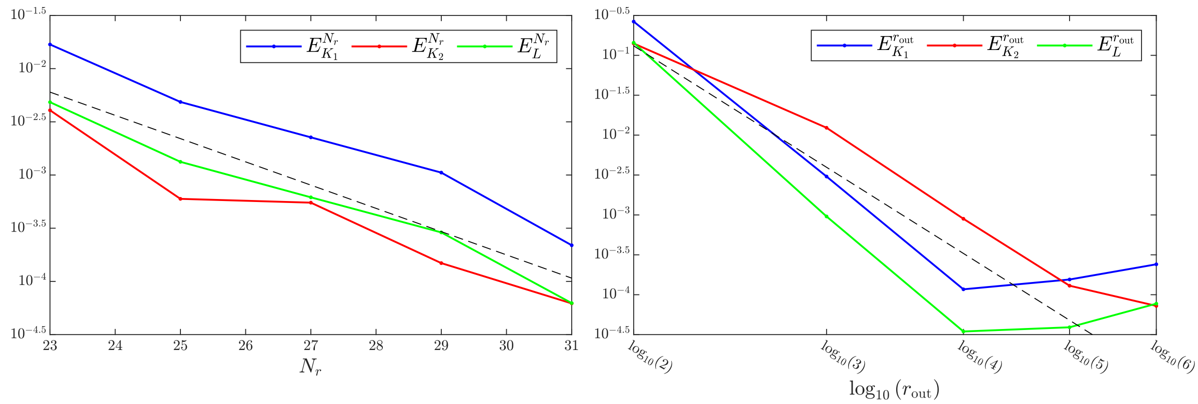

FIG. D2. Left panel: log plots of $E^{N_r}_{K_1}$, $E^{N_r}_{K_2}$ and $E^{N_r}_{L}$ as functions of N_r. The parameters $N_z = 81$, $N_s = 20$ and $r_{\text{out}} = 5$ are fixed. The dashed line is a linear approximant to the average error calculated using a least squares regression method, the gradient of which is approximately -0.22. Right panel: log-log plots of $E^{r_{\text{out}}}_{K_1}$, $E^{r_{\text{out}}}_{K_2}$ and $E^{r_{\text{out}}}_{L}$ as functions of r_{out}. The parameters $N_z = 81$, $N_s = 20$ and $N_r = 31$ are fixed. The dashed line is a linear approximant to the average error for $r_{\text{out}} \leq 5$ calculated using a least squares regression method, the gradient of which is approximately -8.64.

to an algebraic decay), followed by a small increase. Importantly, this increase only occurs after the error introduced by the discretization of r using 31 Chebyshev points surpasses the error introduced by truncating the domain at r_{out}. This indicates that the error increase at $r_{\text{out}} \approx 5$ is due to the grid resolution on the larger domain no longer being fine enough to resolve the radial structures. It is reasonable however, to conclude that the errors decay algebraically as r_{out} is increased, assuming that we are able to resolve radial structures with a fine enough Chebyshev discretization. The dashed line in this panel is calculated using a least squares regression method based on the average of the three errors for $r_{\text{out}} \leq 5$, and has a gradient of approximately -8.64, indicating that the errors decay as $E^{r_{\text{out}}}_{K_1}, E^{r_{\text{out}}}_{K_2}, E^{r_{\text{out}}}_{L} \sim r_{\text{out}}^{-8.64}$.

c. *Convergence in the vertical domain*

Demonstrating the convergence of the transilient kernels as a function of the number of vertical grid points N_z is somewhat more challenging since the size of the discretized matrices increases at each iteration. Instead, we analyse the convergence of the individual functions $K_{1,j}(z)$, $K_{2,j}(z)$ and $L_j(z)$ in the expansions (47a–47c) by projecting them onto a suitable basis. Since all of the functions vanish on $z = 0, 1$ for all $j = 0, 1, 2...$, we opt to use a Fourier sine series. That is, we

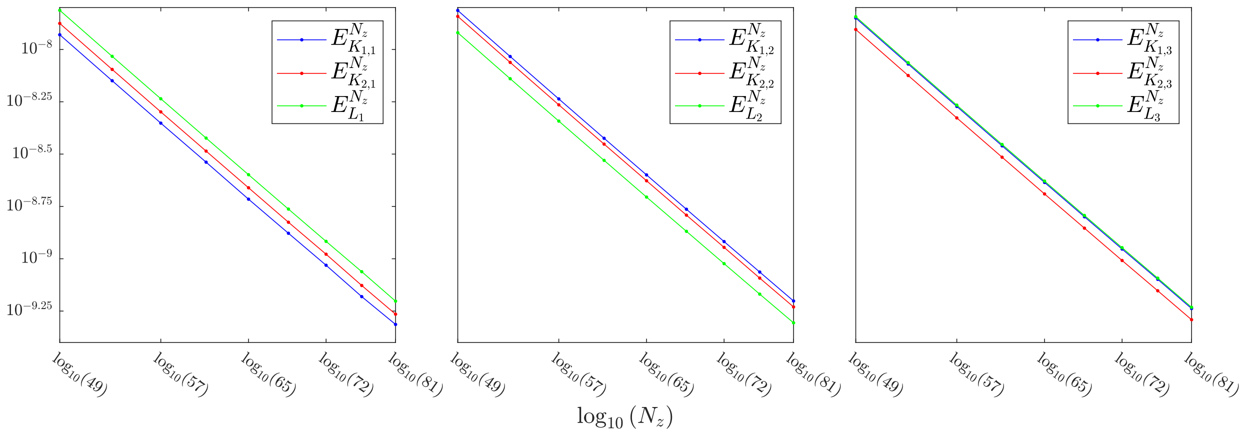

FIG. D3. log-log plots of the errors $E_{K_{1,j}}^{N_z}$, $E_{K_{2,j}}^{N_z}$ and $E_{L_j}^{N_z}$ for $j = 1, 2, 3$ (left-right). A least squares regression analysis shows that all curves in each plot may be approximated by a linear function with gradient -6.35 (approximants are omitted from the figure).

expand the functions as, for example

$$K_{1,j}(z) = \sum_{n=1}^{\infty} a_{j,n} \sin(n\pi z), \tag{D4}$$

from which the coefficients can be calculated using the orthogonality of the basis functions. Now we define

$$\mathbf{a}_j^{N_z} = \left(a_{j,1}, a_{j,2}, ..., a_{j,10}\right)^T, \tag{D5}$$

as the vector of the first 10 coefficients, where each entry is calculated numerically using N_z vertical grid points. This allows us to introduce the step-wise error as

$$E_{K_{1,j}}^{N_z} = \frac{\|\mathbf{a}_j^{N_z} - \mathbf{a}_j^{N_z-4}\|_{L^2}}{\|\mathbf{a}_j^{N_z}\|_{L^2}}, \tag{D6}$$

with $E_{K_{2,j}}^{N_z}$ and $E_{L_j}^{N_z}$ defined analogously.

Fig. D3 shows log-log plots of $E_{K_{1,j}}^{N_z}$, $E_{K_{2,j}}^{N_z}$ and $E_{L_j}^{N_z}$ for $j = 1, 2, 3$, which show a clear algebraic decay in the step-wise error. All lines in the plot have a gradient of approximately -6.35 indicating that the errors decay as $E_{K_{1,j}}^{N_z}, E_{K_{2,j}}^{N_z}, E_{L_j}^{N_z} \sim N_z^{-6.35}$. This decay is also observed for values of $j > 3$, and when the number of coefficients in (D5) is chosen to be greater than 10 (as long as the basis vectors can be resolved on the Chebyshev grid with a high enough accuracy).

References

Arakawa, A., 2004: The cumulus parameterization problem: Past, present, and future. *Journal of Climate*, **17 (13)**, 2493 – 2525, https://doi.org/10.1175/1520-0442(2004)017⟨2493:RATCPP⟩2.0.CO;2, URL https://journals.ametsoc.org/view/journals/clim/17/13/1520-0442_2004_017_2493_ratcpp_2.0.co_2.xml.

Arakawa, A., and W. H. Schubert, 1974: Interaction of a cumulus cloud ensemble with the large-scale environment, part i. *Journal of Atmospheric Sciences*, **31 (3)**, 674 – 701, https://doi.org/10.1175/1520-0469(1974)031⟨0674:IOACCE⟩2.0.CO;2, URL https://journals.ametsoc.org/view/journals/atsc/31/3/1520-0469_1974_031_0674_ioacce_2_0_co_2.xml.

Benilov, E. S., 2000: Waves on the beta-plane over sparse topography. *Journal of Fluid Mechanics*, **423**, 263–273, https://doi.org/10.1017/S0022112000001890.

Bhamidipati, N., A. Souza, and G. Flierl, 2020: Turbulent mixing of a passive scalar in the ocean mixed layer. *Ocean Modelling*, **149**, 101 615, https://doi.org/10.1016/j.ocemod.2020.101615.

Biello, J. A., and A. J. Majda, 2005: A new multiscale model for the Madden–Julian oscillation. *Journal of the Atmospheric Sciences*, **62 (6)**, 1694 – 1721, https://doi.org/10.1175/JAS3455.1, URL https://journals.ametsoc.org/view/journals/atsc/62/6/jas3455.1.xml.

Biello, J. A., and A. J. Majda, 2010: Intraseasonal multi-scale moist dynamics of the tropical atmosphere. *Communications in Mathematical Sciences*, **8 (2)**, 519 – 540, https://doi.org/cms/1274816893, URL https://doi.org/.

Boyd, J. P., 2001: *Chebyshev and Fourier Spectral Methods*. New York.

Cheng, B., M. J. P. Cullen, J. G. Esler, J. Norbury, M. R. Turner, J. Vanneste, and J. Cheng, 2017: A model for moist convection in an ascending atmospheric column. *Quarterly Journal of the Royal Meteorological Society*, **143 (708)**, 2925–2939, https://doi.org/https://doi.org/10.1002/qj.3144, URL https://rmets.onlinelibrary.wiley.com/doi/abs/10.1002/qj.3144, https://rmets.onlinelibrary.wiley.com/doi/pdf/10.1002/qj.3144.

Collins, S. N., R. S. James, P. Ray, K. Chen, A. Lassman, and J. Brownlee, 2013: Grids in numerical weather and climate models. *Climate Change and Regional/Local Responses*, IntechOpen, chap. 4, https://doi.org/10.5772/55922, URL https://doi.org/10.5772/55922.

Craig, P., 1987: Solutions for internal tidal generation over coastal topography. *Journal of Marine Research*, **45 (1)**, 83–105.

Emanuel, K. A., 1991: A scheme for representing cumulus convection in large-scale models. *Journal of Atmospheric Sciences*, **48 (21)**, 2313 – 2329, https://doi.org/https://doi.org/10.1175/1520-0469(1991)048⟨2313:ASFRCC⟩2.0.CO;2, URL https://journals.ametsoc.org/view/journals/atsc/48/21/1520-0469_1991_048_2313_asfrcc_2_0_co_2.xml.

Forster, C., A. Stohl, and P. Seibert, 2007: Parameterization of convective transport in a Lagrangian particle dispersion model and its evaluation. *Journal of Applied Meteorology and Climatology*, **46 (4)**, 403 – 422, https://doi.org/10.1175/JAM2470.1, URL https://journals.ametsoc.org/view/journals/apme/46/4/jam2470.1.xml.

Garrett, C., and E. Kunze, 2007: Internal tide generation in the deep ocean. *Annual Review of Fluid Mechanics*, **39 (1)**, 57–87, https://doi.org/10.1146/annurev.fluid.39.050905.110227, URL https://doi.org/10.1146/annurev.fluid.39.050905.110227, https://doi.org/10.1146/annurev.fluid.39.050905.110227.

Gill, A. E., 1980: Some simple solutions for heat-induced tropical circulation. *Quarterly Journal of the Royal Meteorological Society*, **106 (449)**, 447–462, https://doi.org/https://doi.org/10.1002/qj.49710644905, URL https://rmets.onlinelibrary.wiley.com/doi/abs/10.1002/qj.49710644905, https://rmets.onlinelibrary.wiley.com/doi/pdf/10.1002/qj.49710644905.

Gill, A. E., 1982: *Atmosphere-Ocean Dynamics*. Academic Press New York, xv, 662 p. : pp., URL http://www.loc.gov/catdir/toc/els031/82008704.html.

Goldsmith, E., and J. Esler, 2021: Wave propagation in rotating shallow water in the presence of small-scale topography. *Journal of Fluid Mechanics*, **923**, A24, https://doi.org/10.1017/jfm.2021.573.

Gregory, D., 2002: The mass-flux approach to the parametrization of deep convection. ECMWF, URL https://www.ecmwf.int/node/16956.

Gregory, D., and P. R. Rowntree, 1990: A mass flux convection scheme with representation of cloud ensemble characteristics and stability-dependent closure. *Monthly Weather Review*, **118 (7)**, 1483 – 1506, https://doi.org/10.1175/1520-0493(1990)118⟨1483:AMFCSW⟩2.0.CO;2, URL https://journals.ametsoc.org/view/journals/mwre/118/7/1520-0493_1990_118_1483_amfcsw_2_0_co_2.xml.

Holton, J. R., and G. J. Hakim, 2013: Chapter 11 - tropical dynamics. *An Introduction to Dynamic Meteorology*, 5th ed., Academic Press, Boston, 377–411, https://doi.org/https://doi.org/10.1016/B978-0-12-384866-6.00011-8, URL https://www.sciencedirect.com/science/article/pii/B9780123848666000118.

Holtslag, A. A., 2003: Atmospheric turbulence. *Encyclopedia of Physical Science and Technology*, 3rd ed., Academic Press, New York, 707–719, https://doi.org/https://doi.org/10.1016/B0-12-227410-5/00039-9, URL https://www.sciencedirect.com/science/article/pii/B0122274105000399.

Igel, M. R., and J. A. Biello, 2020: The nontraditional coriolis terms and tropical convective clouds. *Journal of the Atmospheric Sciences*, **77 (12)**, 3985 – 3998, https://doi.org/10.1175/JAS-D-20-0024.1, URL https://journals.ametsoc.org/view/journals/atsc/77/12/JAS-D-20-0024.1.xml.

Kelly, S. M., 2016: The vertical mode decomposition of surface and internal tides in the presence of a free surface and arbitrary topography. *Journal of Physical Oceanography*, **46 (12)**, 3777 – 3788, https://doi.org/10.1175/JPO-D-16-0131.1, URL https://journals.ametsoc.org/view/journals/phoc/46/12/jpo-d-16-0131.1.xml.

Kelly, S. M., J. D. Nash, and E. Kunze, 2010: Internal-tide energy over topography. *Journal of Geophysical Research: Oceans*, **115 (C6)**, https://doi.org/https://doi.org/10.1029/2009JC005618, URL https://agupubs.onlinelibrary.wiley.com/doi/abs/10.1029/2009JC005618, https://agupubs.onlinelibrary.wiley.com/doi/pdf/10.1029/2009JC005618.

Kuell, V., and A. Bott, 2022: A nonlocal three-dimensional turbulence parameterization (NLT3D) for numerical weather prediction models. *Quarterly Journal of the Royal Meteorological Society*, **148 (742)**, 117–140, https://doi.org/https://doi.org/10.1002/qj.4195.

Li, Y., and C. C. Mei, 2014: Scattering of internal tides by irregular bathymetry of large extent. *Journal of Fluid Mechanics*, **747**, 481–505, https://doi.org/10.1017/jfm.2014.159.

Ling, J., and C. Zhang, 2013: Diabatic heating profiles in recent global reanalyses. *Journal of Climate*, **26 (10)**, 3307 – 3325, https://doi.org/10.1175/JCLI-D-12-00384.1, URL https://journals.ametsoc.org/view/journals/clim/26/10/jcli-d-12-00384.1.xml.

Majda, A., and R. Klein, 2003: Systematic multiscale models for the tropics. *Journal of the Atmospheric Sciences*, **60**, 393–408, https://doi.org/10.1175/1520-0469(2003)060⟨0393:SMMFTT⟩2.0.CO;2.

Matsuno, T., 1966: Quasi-geostrophic motions in the equatorial area. *Journal of the Meteorological Society of Japan. Ser. II*, **44 (1)**, 25–43, https://doi.org/10.2151/jmsj1965.44.1_25.

Motsa, S., V. Magagula, and P. Sibanda, 2014: A bivariate Chebyshev spectral collocation quasi-linearization method for nonlinear evolution parabolic equations. *The Scientific World Journal*, **vol 2014**, https://doi.org/10.1155/2014/581987.

Muzara, H., S. Shateyi, and G. T. Marewo, 2018: On the bivariate spectral quasi-linearization method for solving the two-dimensional Bratu problem. *Open Physics*, **16 (1)**, 554–562, https://doi.org/doi:10.1515/phys-2018-0072, URL https://doi.org/10.1515/phys-2018-0072.

Ogura, Y., and N. A. Phillips, 1962: Scale analysis of deep and shallow convection in the atmosphere. *Journal of the Atmospheric Sciences*, **19 (2)**, 173 – 179, https://doi.org/10.1175/1520-0469(1962)019⟨0173:SAODAS⟩2.0.CO;2, URL https://journals.ametsoc.org/view/journals/atsc/19/2/1520-0469_1962_019_0173_saodas_2_0_co_2.xml.

Olbers, D., J. Willebrand, and C. Eden, 2012: *Ocean Dynamics*. https://doi.org/10.1007/978-3-642-23450-7.

Ooyama, K., 1971: A theory on parameterization of cumulus convection. *Journal of the Meteorological Society of Japan. Ser. II*, **49A**, 744–756, https://doi.org/10.2151/jmsj1965.49A.0_744.

Plumb, R. A., and A. Y. Hou, 1992: The response of a zonally symmetric atmosphere to subtropical thermal forcing: Threshold behavior. *Journal of the Atmospheric Sciences*, **49 (19)**, 1790 – 1799, https://doi.org/10.1175/1520-0469(1992)049⟨1790:TROAZS⟩2.0.CO;2, URL https://journals.ametsoc.org/view/journals/atsc/49/19/1520-0469_1992_049_1790_troazs_2_0_co_2.xml.

Radko, T., 2022a: Spin-down of a baroclinic vortex by irregular small-scale topography. *Journal of Fluid Mechanics*, **953**, A7.

Radko, T., 2022b: Spin-down of a barotropic vortex by irregular small-scale topography. *Journal of Fluid Mechanics*, **944**, A5.

Rayleigh, L., 1892: On the influence of obstacles arranged in rectangular order upon the properties of a medium. *Philosophical Magazine*, **34 (211)**, 481–502, https://doi.org/10.1080/14786449208620364.

Romps, D. M., and Z. Kuang, 2011: A transilient matrix for moist convection. *Journal of the Atmospheric Sciences*, **68 (9)**, 2009 – 2025, https://doi.org/10.1175/2011JAS3712.1, URL https://journals.ametsoc.org/view/journals/atsc/68/9/2011jas3712.1.xml.

Shnirelman, A., 1993: The lattice theory and the flows of an ideal incompressible fluid. *Russian journal of mathematical physics*, **1**, 105–114.

Shnirelman, A., 2013: On the long time behavior of fluid flows. *Procedia IUTAM*, **7**, 151–160, https://doi.org/https://doi.org/10.1016/j.piutam.2013.03.018, URL https://www.sciencedirect.com/science/article/pii/S2210983813000424, iUTAM Symposium on Topological Fluid Dynamics: Theory and Applications.

Slingo, J., and Coauthors, 1994: Mean climate and transience in the tropics of the ugamp gcm: Sensitivity to convective parametrization. *Quarterly Journal of the Royal Meteorological Society*, **120 (518)**, 881–922, https://doi.org/https://doi.org/10.1002/qj.49712051807, URL https://rmets.onlinelibrary.wiley.com/doi/abs/10.1002/qj.49712051807, https://rmets.onlinelibrary.wiley.com/doi/pdf/10.1002/qj.49712051807.

Smith, S. G. L., and W. R. Young, 2002: Conversion of the barotropic tide. *Journal of Physical Oceanography*, **32 (5)**, 1554 – 1566, https://doi.org/10.1175/1520-0485(2002)032⟨1554:COTBT⟩2.0.CO;2, URL https://journals.ametsoc.org/view/journals/phoc/32/5/1520-0485_2002_032_1554_cotbt_2.0.co_2.xml.

Stull, R. B., 1984: Transilient turbulence theory. part I: The concept of eddy-mixing across finite distances. *Journal of the Atmospheric Sciences*, **41 (23)**, 3351 – 3367, https://doi.org/10.1175/1520-0469(1984)041⟨3351:TTTPIT⟩2.0.CO;2, URL https://journals.ametsoc.org/view/journals/atsc/41/23/1520-0469_1984_041_3351_tttpit_2_0_co_2.xml.

Trefethen, L. N., 2000: *Spectral Methods in MATLAB*. SIAM, Philadelphia.

Vanneste, J., 2000a: Enhanced dissipation for quasi-geostrophic motion over small-scale topography. *Journal of Fluid Mechanics*, **407**, 105–122.

Vanneste, J., 2000b: Rossby wave frequency change induced by small-scale topography. *Journal of Physical Oceanography*, **30 (7)**, 1820–1826.

Vanneste, J., 2003: Nonlinear dynamics over rough topography: homogeneous and stratified quasi-geostrophic theory. *J. Fluid Mech.*, **474**, 299–318.

Villafuerte, M. Q., J. C. R. Lambrento, K. I. Hodges, F. T. Cruz, T. A. Cinco, and G. T. Narisma, 2021: Sensitivity of tropical cyclones to convective parameterization schemes in RegCM4. *Climate Dynamics*, **56 (5-6)**, 1625–1642, https://doi.org/10.1007/s00382-020-05553-3.

Wirth, V., 1998: Thermally forced stationary axisymmetric flow on the f plane in a nearly frictionless atmosphere. *Journal of the Atmospheric Sciences*, **55 (19)**, 3024 – 3041, https://doi.org/10.1175/1520-0469(1998)055⟨3024:TFSAFO⟩2.0.CO;2, URL https://journals.ametsoc.org/view/journals/atsc/55/19/1520-0469_1998_055_3024_tfsafo_2.0.co_2.xml.

Wirth, V., and T. J. Dunkerton, 2006: A unified perspective on the dynamics of axisymmetric hurricanes and monsoons. *Journal of the Atmospheric Sciences*, **63 (10)**, 2529 – 2547, https://doi.org/10.1175/JAS3763.1, URL https://journals.ametsoc.org/view/journals/atsc/63/10/jas3763.1.xml.

Wood, R., and M. Mcintyre, 2009: A general theorem on angular-momentum changes due to potential vorticity mixing and on potential-energy changes due to buoyancy mixing. *Journal of the Atmospheric Sciences*, **67**, https://doi.org/10.1175/2009JAS3293.1.